Globular Cluster Bimodality in Isolated Elliptical Galaxies

Master's Thesis
University of Turku
Department of Physics and Astronomy
Astronomy
May 2013
Alabi Adebusola Bamidele
Supervised by:
Dr. Ricardo Salinas
Prof. Harry Lehto

TURUN YLIOPISTO
Department of Physics and Astronomy

ALABI, Adebusola Bamidele: Globular Cluster Bimodality in Isolated Elliptical Galaxies
Master's Thesis, 62 pages
Astronomy
May 2013

This thesis presents deep photometry of the globular cluster (GC) system of three isolated elliptical galaxies: NGC 3962, NGC 2865 and NGC 2271. Due to the scarcity of isolated ellipticals in the local universe, little is known about the properties of globular cluster systems (GCS) in under-dense environments. Using data obtained from the Gemini South telescopes in the g' and i' filter passbands, we have determined the color and radial distributions for these GCS.

We find bimodal color distributions in the GCS of all the isolated elliptical galaxies in our sample, with NGC 2865 showing evidence of a third mode. The peak colors of the metal-rich sub-populations in all our GCS are slightly redder than in results obtained for GCS of similar mass galaxies in denser environments. The three GCS we have studied are dominated by GCs belonging to the metal-poor sub-population, a result clearly at odds with predictions from some hierarchical based models where red GCs are expected to be more abundant.

No difference is found in the spatial distribution of the blue and red sub-populations in our sample compared to results from denser environments. The blue GCs have a more extended radial distribution and the red are more centrally concentrated. We obtained shallow, negative average GC color gradients in the three galaxies studied.

We report the detection of a population of ultra-compact dwarf (UCD) candidates in NGC 3962. Spectroscopic studies to confirm their membership is ongoing.

keywords: globular clusters, elliptical galaxies.

Contents

List of Abbreviations **3**

1 Introduction **5**

1.1 Globular clusters 5

1.2 Globular Cluster Systems 7

1.2.1 Globular Cluster Luminosity Function 8

1.2.2 Specific Frequency 8

1.2.3 Color Bimodality 9

1.3 Theories of Globular Cluster System Formation 12

1.3.1 Major merger model 12

1.3.2 Dissipational collapse model 13

1.3.3 Dissipationless accretion model 14

1.4 Predictions of models for low density environments 15

1.5 Isolated Elliptical Galaxies 17

1.6 Isolated Elliptical Galaxy Samples 18

1.7 The Galaxy Sample 19

1.7.1 NGC 3962 19

1.7.2 NGC 2865 20

1.7.3 NGC 2271 21

2 Data and Reduction **22**

2.1 Data 22

2.2 Image reduction 23

2.3 Object Detection and Photometry 24
2.4 Photometric Calibrations 26
2.5 Completeness Test 27
2.6 Object Classification 28
2.7 Globular cluster candidate selection 31
2.8 Contamination from Background Galaxies 31

3 Results **33**

3.1 Color distribution of globular clusters 35
3.2 Radial distribution of globular clusters 41

4 Discussion **45**

4.1 Host galaxy properties versus globular cluster properties 45
4.2 Effects of galaxy evolution on GCS in isolated elliptical galaxies 52

5 Summary and conclusions **54**

List of Abbreviations

ACS Advanced Camera for Surveys

CMD Color magnitude diagram

FOV field of view

GC Globular cluster

GCLF Globular cluster luminosity function

GCS Globular cluster system

GMM Gaussian Mixture Modelling

GMOS Gemini multi-object spectrograph

GSA Gemini Science Archive

IRAF Image Reduction and Analysis Facility

LEDA Lyon-Meudon Extragalactic Database

LF luminosity function

MW Milky Way

NIR near-infrared

PSF point spread function

SDSS Sloan Digital Sky Survey

SSP simple stellar population

TOM turnover magnitude

UCD Ultra-compact dwarf

WHDF William Herschel Deep Field

Chapter 1

Introduction

Astronomers try to answer questions like how did the celestial objects we see today form, how long have they been around, how have they evolved in time? Such puzzles are resolved by proposing hypothesis and models which often times do not adequately describe the entire spectrum of the observed properties of these objects. The ultimate goal is to find the "right" model that accounts for all what we know about our object of interest. This thesis uses the globular cluster systems of some isolated elliptical galaxies to provide clues that would help in answering these questions.

1.1 Globular clusters

Star clusters are useful tools in answering some of these fundamental questions and in constraining the several models. Stars in a cluster have the same age, the same initial chemical composition and are roughly at the same distance from the earth (differing only in their masses), forming rare astrophysical "laboratories". A ***globular cluster*** (GC) is a roughly spherical group of stars, orbiting a galactic core, tightly bound by gravity with high stellar density towards the center. The stars however have different masses and are in different evolutionary phases. GCs are the oldest, visible stellar structures in the universe. A typical GC has $\sim 10^4 - 10^6$ stars concentrated within $\sim 10^3$ pc^3. They are thus compact objects with typical half-light radii of a few pc. GCs have been found around galaxies of all morphological types over a wide range of galaxy luminosities (brighter than $\sim M_B = -15$). The Milky Way

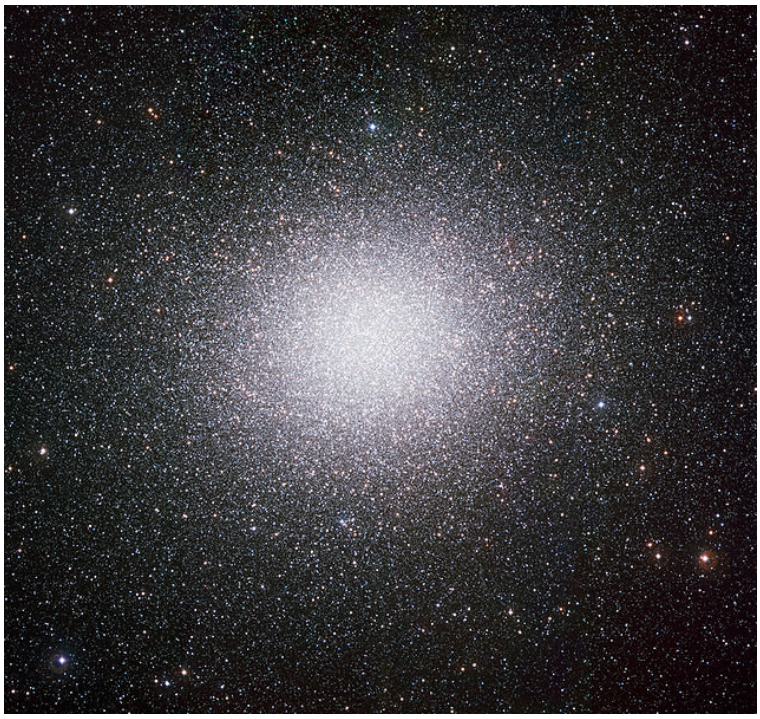

Figure 1: The GC ω Centauri. Credit: ESO

(MW) has ∼150 GCs, Andromeda (M31) has ∼400 GCs, Virgo A (M87) has ∼13,000 GCs while Fornax dwarf spheroidal has 5 GCs (Kissler-Patig et al. 1997; Ashman & Zepf 1998). Fig. 1 shows the GC ω Centauri, the largest and brightest GC orbiting the MW. Most GCs probably formed at the same time as their host galaxies (Brodie & Strader 2006). Since they are the oldest objects that survived the dynamical evolution of the galaxy system, they are therefore relics with unique fossil records of the conditions during galaxy formation and early evolution. Also, GCs are good tracers of the star formation histories of their host galaxies (Larsen et al. 2001). Major star formation epochs are normally accompanied by significant GC formation (Strader et al. 2005). GCs and field stars form during initial proto-galactic cloud collapse and gas-rich major mergers. The number of clusters formed is proportional to the amount of gas involved (Djorgovski & Santiago 1992) and properties of the GCs scale with the properties of the host galaxy e.g number of GCs has a very tight correlation with the total galaxy stellar mass (Rhode & Zepf 2004). Hence they can be studied to understand

the chemical enrichment history of spheroids and halos.

Historically, the study of GCs was used to show that the MW is not heliocentric. Shapley (e.g 1918), from a series of studies of the GCs in MW, showed that the Sun was offset from the center of the spherical distribution of GCs by ~ 15 kpc. The current estimate for the offset is $\sim 7.6 - 8.7$ kpc (Gillessen et al. 2009). GCs are also among the first objects used to establish the distance scale of the Universe. The peak magnitude of the globular cluster luminosity function (GCLF) is an established secondary distance indicator with intrinsic accuracy of the order of ~ 0.2 mag (e.g Rejkuba 2012).

Individual GCs in the Local Group can be characterised with a single age and a single metallicity (since they appear as point sources), indicating that the clusters formed in a single star formation episode (Puzia 2003). There are exceptions however, ω Cen orbiting the MW and Mayall II (G1) orbiting M31 have wide metallicity distributions (multiple star formation episodes). Alternatively, these objects have been described as stripped dwarf galaxies (e.g. Zinnecker et al. 1988; Hilker & Richtler 2000; Meylan et al. 2001; Bekki & Freeman 2003). The GCs NGC 2808, NGC 1851, NGC 2419, Ter 5 and NGC 6656 in our MW also show this wide metallicity distribution and there is increasing evidence that virtually all GCs show some level of chemical composition inhomogeneity (Valcarce & Catelan 2011; Bragaglia et al. 2013).

1.2 Globular Cluster Systems

The Globular cluster system (GCS) of an elliptical galaxy is the ensemble of all the old star clusters (>= 10 Gyr) found in its spheroid and halo region. Most Galactic GCs are old with mean age of ~ 13 Gyr and dispersion of 2-3 Gyr (e.g. Krauss & Chaboyer 2003). By mass, GCS constitute $\sim 0.25\%$ of the total stellar mass of the host galaxy and for all types of galaxy morphologies, the number of GCs normalised to the total baryonic mass of the host

gives a constant value of $\sim 0.25\%$ (McLaughlin 1999). Below is a brief description of the global properties of GCS.

1.2.1 Globular Cluster Luminosity Function

The relative number of GCs per unit magnitude of a GCS gives the GCLF which can be described by either a Gaussian or a t-distribution ($df = 5$) (Secker 1992). The GCLF is characterised by the dispersion and the turnover magnitude (TOM). GCLFs have a universal shape in all GCS studied, with an asymmetry in the form of a longer tail towards the faint magnitude end. This is due to the preferential erosion of low mass clusters during the dynamical evolution of the galaxy (Harris & Pudritz 1994). The TOM of the GCLF is almost universal (for all observed GCS and different morphology) with a mean magnitude of $\mathrm{M_v} = -7.4 \pm 0.2$ and a dispersion $\sigma = 1.2$ for MW and M31 (Ashman & Zepf 1998). The dispersion of the distribution is linked to the absolute magnitude of the host galaxy (Jordán et al. 2006).

1.2.2 Specific Frequency

The specific frequency, S_N, of a GCS is the number of GCs per unit luminosity of the host galaxy and it is a description of how rich the GCS is. It is defined by

$$S_N = N_{\mathrm{GC}} \times 10^{0.4(M_V+15)}$$

where N_{GC} is the total number of GCs and M_V is the galaxy's absolute V-band magnitude such that a $M_V = -15$ galaxy with one GC has a S_N equal to one. Dwarf and large elliptical galaxies have higher S_N than spirals (e.g. Forbes 2005) since they have different mass-to-light ratios and total stellar mass is not used for the normalisation. However, for galaxies hosting more than 10000 GCs, M_V is easily underestimated due to their very extended stellar halos

as shown in results obtained by McLaughlin et al. (1995); Wehner et al. (2008) and Richtler et al. (2011) for NGC 3311. In a galaxy that has no interaction history, the S_N gives the formation efficiency of GCs relative to field stars and how well they survived. Harris & van den Bergh (1981) reported values in the range $2 < S_N < 10$ for elliptical galaxies. M87, the central galaxy in the Virgo Cluster, has a high value $S_N = 12.6 \pm 0.8$ (Peng et al. 2006). This suggests the influence of environment in GC formation. High S_N galaxies have been identified as brightest galaxies or second brightest galaxies in clusters.

1.2.3 Color Bimodality

Bimodality has been observed in the optical color distribution of nearly every massive galaxy studied with accurate and deep enough photometry (Brodie & Strader 2006). Color bimodality is the most important defining feature in modern GC studies. Histograms of GC color generally have two peaks (blue and red peaks) which are found at similar colors for most galaxies in the same filter system. This implies the presence of two sub-populations of GCs in the system which either formed at different epochs and/or through different mechanisms. In Fig. 2, bimodality is clearly obvious in the color-magnitude diagram (CMD) of NGC 1399 obtained from wide-field photometry using filters in the Washington system (Dirsch et al. 2003).

Bimodality can be attributed to age and/or metallicity differences between the sub-populations, though spectroscopic studies have shown that it is mainly due to metallicity difference between the sub-populations. The blue and red peaks correspond to the metal-poor and metal-rich sub-populations (e.g. Puzia et al. 2005; Strader et al. 2006; Brodie et al. 2012; Usher et al. 2012).

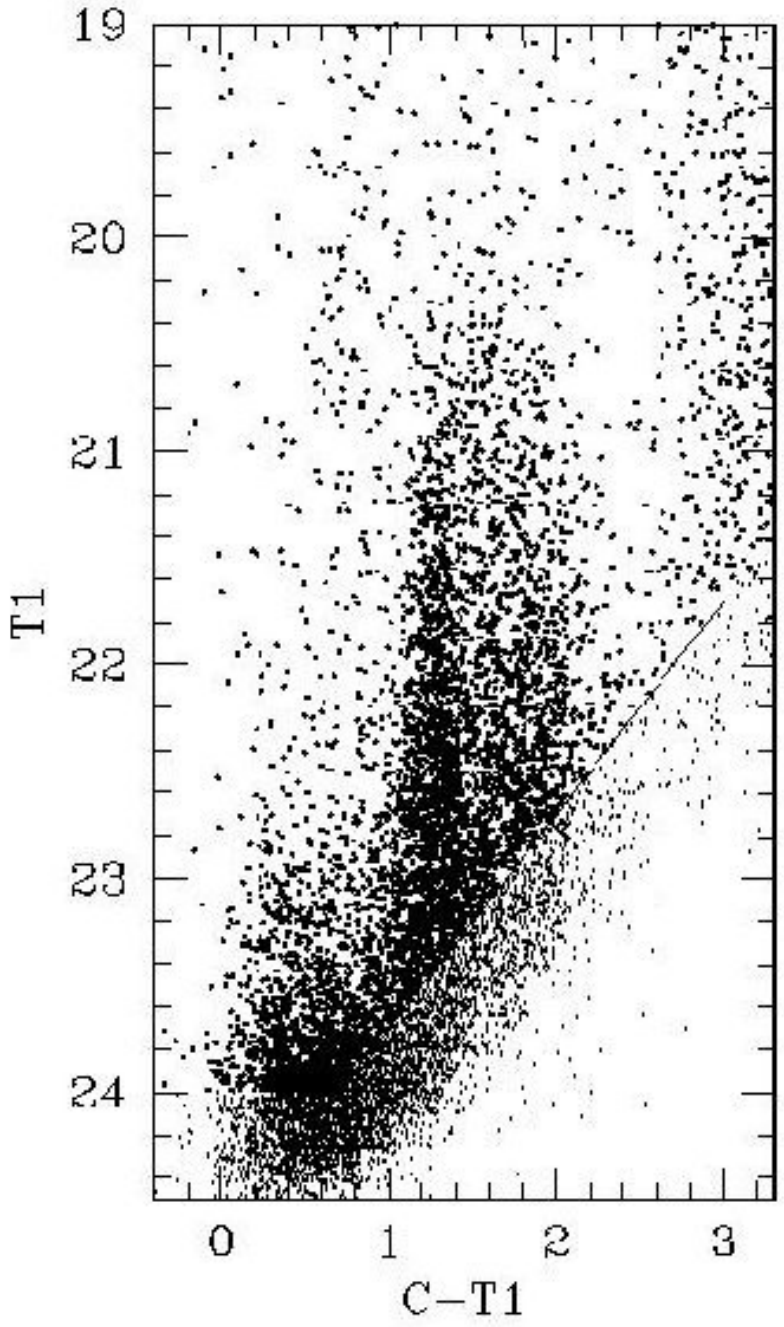

Figure 2: CMD of detected objects in the field of NGC 1399 using filters in the Washington system. The line corresponds to limiting magnitude of the photometry (Dirsch et al. 2003).

Bimodality in metallicity has been observed in spectroscopic studies of the MW (e.g. Zinnecker et al. 1988; Bica et al. 2006) and M31 our spiral neighbour (e.g. Barmby et al. 2000)

though it is less pronounced in M31 (Caldwell et al. 2011). In the MW, the metal-poor GCs are found in the halo, at large galactocentric radii (Armandroff & Zinn 1988) while the metal-rich GCs are associated with the bulge (Côté et al. 1998). However, knowledge of GC color distributions in spiral galaxies, especially outside the Local Group, is sparse (Puzia 2003). This is due to contamination from the young star cluster populations, crowding and extinction correction problems, which are much more severe in spirals. Bimodality is thus easier to study in elliptical and S0 galaxies because of the large numbers of globular clusters in their halos.

Several studies (e.g. Forbes et al. 1997; Larsen et al. 2001; Forbes & Forte 2001) showed that there is a strong correlation between the mean color of the red sub-population and the host galaxy luminosity and also with galaxy halo-star color. This is evidence that GCs are tracers of the chemical abundance evolution of the star formation and assembly processes that shaped galaxies over cosmic time. While metallicity may be the most important driver of GCS color bimodality, age effects, especially outside the Local Group, are also important (Puzia 2003).

Richtler (2006), Yoon et al. (2006, 2011a,b) however suggested that a broad, single-peaked metallicity distribution, presumably as a result of continuous chemical enrichment, can produce color bimodality due to non-linearity of metallicity-color relation, without invoking two distinct sub-populations. These studies suggest that color distributions do not translate directly into metallicity distribution. They showed that non-linear color-metallicity relations caused by the hot horizontal branch stars may also transform a unimodal metallicity distribution into a bimodal optical color distribution. Chies-Santos et al. (2012) using optical/near-infrared (NIR) color distributions of the GC systems in 14 E/S0 galaxies concluded that a bimodal optical color distribution is not necessarily an indication of an underlying bimodal metallicity distribution. However, Brodie et al. (2012), using the GCS of NGC 3115, showed that color and CaT index (a metallicity proxy as it correlates closely with metallicity) are

bimodal, lending more weight to the evidence, from direct metallicity distribution functions, that multiple GC metallicity sub-populations are common.

1.3 Theories of Globular Cluster System Formation

Several models with different variants attempt to describe the formation of the large GCS observed in elliptical galaxies within the hierarchical framework. Generally these models can be grouped into three broad classes: gas-rich major merger, multi-phase dissipational collapse and dissipationless accretion.

1.3.1 Major merger model

Ashman & Zepf (1992) proposed that in the gas-rich major mergers of spiral galaxies, new GCs are formed such that the GCS of the new elliptical galaxy is made up of metal-poor GCs from the progenitor spirals and young, metal-rich GCs are formed during the merger. The model is unique in that it predicted bimodality in GCS before it was observed (Ostrov et al. 1993; Zepf & Ashman 1993). Large number of young massive star clusters (YMCs) have been observed in the famous Antennae galaxy-galaxy merger (Whitmore & Schweizer 1995) and in several other star forming events - in NGC 1275 (Holtzman et al. 1992), NGC 3256 (Zepf et al. 1999, etc) and they are believed to be the progenitors of globular clusters, though the fraction of YMCs that survive to become GCs is not well constrained (Portegies Zwart et al. 2010). The luminosity function (LF) of YMCs is well described by a power-law

$$\frac{dN}{dL} \sim L^{\alpha}$$

with $\alpha \sim 2$ (Whitmore & Schweizer 1995). How the power-law LF is converted to the observed log-normal GCLF is however not properly understood especially considering the mechanism

of dynamical interactions of a star cluster with its host galaxy (Fall & Zhang 2001).

Even though there are observational evidences for major mergers, several problems are associated with the model if it is considered as the sole process responsible for bimodality. For example, the model predicts that more massive ellipticals with higher S_N should have larger metal-rich sub-population since new metal-rich GCs are formed in the spiral-spiral merger. However, Forbes (2005) showed that there is a correlation between S_N and the fraction of metal-poor GCs, such that the highest S_N galaxies also have the highest proportion of metal-poor GCs. Also, on the average, the metal-poor GC sub-populations of spirals have lower metallicities than those of massive ellipticals (Strader et al. 2004). There has to be some other mechanism(s) responsible for this observed shift.

1.3.2 Dissipational collapse model

Due to the inconsistency of the observed S_N and color distribution of the GCS in massive ellipticals with the predictions of the major merger model, Forbes et al. (1997) suggested a multiphase dissipational collapse where metal-poor clusters are first formed at high redshift $z > 5$ but not before $z \sim 12$ in low-mass proto-galaxies during initial galaxy formation after which star formation is truncated. Metal-rich clusters are then formed when star formation resumes and gas re-collapses. The star formation truncation at high redshift lasts for a few Gyrs and it has been explained in terms of the cosmic reionization epoch. Beasley et al. (2002) proposed a hybrid, semi-analytic galaxy formation model using cosmological formation simulations based on the semi-analytic model of Cole et al. (2000) assuming that "GCs form contemporaneously with the star formation occurring in proto-galactic disc, and during major mergers involving star formation". This would produce two sub-populations of GCs made from gas which has undergone different levels of chemical enrichment: a metal-poor GC sub-population would be formed in the cold gas of the proto-galactic disc and a metal-rich sub-population would be formed during gas-rich merging.

Artificial truncation of the formation of metal-poor GCs at $z \sim 5$ is necessary to prevent the over-production of metal-poor GCs. The GCs would have a significant age-structure with a wide age range (5-12 Gyrs), which would increase for low-luminosity galaxies. Generally, the metal-rich GC sub-populations are younger than the metal-poor GC sub-populations, with mean ages of 9 and 12 Gyrs respectively. Also, the mean ages of the metal-rich GCs would depend on host galaxy luminosity and environment.

1.3.3 Dissipationless accretion model

In the dissipationless accretion model, metal-rich GCs are formed in-situ in a massive seed galaxy, while the metal-poor GCs are acquired in the dissipationless accretion of neighbouring lower-mass galaxies. Since dissipationless accretions involve little or no gas, star formation is absent in this model. Côté et al. (1998) suggests that a substantial part of the GCS of an elliptical galaxy is accreted from neighbouring dwarf galaxies. At the heart of this model is the correlation between the mass of the host galaxy and the mean metallicity of its GCS (Forbes & Forte 2001).

Since the intrinsic GC metallicities of massive protogalaxies are quite high, such galaxies must accrete large numbers of metal-poor GCs from dwarf galaxies to produce bimodality. A large number of metal-poor field stars should also be accreted alongside the metal poor GCs, however, these stars are not observed in the fields of elliptical galaxies (Hilker & Richtler 2000). Also, metal-poor GCs in dwarf galaxies have much lower metallicities than those in massive ellipticals $\sim 0.5 - 0.6$ dex (Strader et al. 2004). Brodie & Strader (2006) suggests that this could be resolved by placing the merger or accretion events at high redshift and allowing for significant gas in the components.

1.4 Predictions of models for low density environments

From these three models it can be concluded that the evolution of galaxies and their GCS is an extended process that is still ongoing, rather than a one-off event in the distant past. If the metal-rich and metal-poor clusters are the result of two separate epoch of star formation, then the metal poor GCs must be older than those that are metal rich. If, however, the bimodal GC sub-populations seen in GCSs are due to the accretion of pre-existing GCs, then the metal-rich and metal-poor GCs should co-evolve and both distributions should be old, with no correlation between metallicity and age.

Most of the studies of GCS in early type galaxies have concentrated on high-density environments where massive ellipticals are very common (e.g. Peng et al. 2006). It is crucial to test these models in GCS of galaxies in under-dense environments where accretion processes is expected to be far less important. Very little is known about GCS in low density environments due to their scarcity in the local Universe. Also, the need for large statistical correction for contaminations from background galaxies make such studies with ground-based imaging more complex.

In the major merger model, blue GCs in elliptical galaxies are inherited directly from spiral progenitors (e.g. Ashman & Zepf 1992), hence it is expected that the number of metal-poor GCs in spirals and ellipticals are similar.

In hierarchical structure formation models, protogalactic clumps in higher density regions start to form GCs earlier than fragments in lower density regions (Elmegreen 2008). This implies that in high density environments, massive galaxies should have more metal-poor GCs that are older per unit mass compared to less massive galaxies in under dense environments.

Also, in hierarchical based major-merger scenario, the blue, metal-poor GCs are expected to have a more extended radial distribution compared to the red, metal-rich sub-population (Brodie & Strader 2006). Due to accretion of metal-poor GCs in the dissipationless accretion

model, they are expected to have a more extended galactocentric distribution. This trend is expected to be more pronounced in giant ellipticals at centers of clusters where capture of dwarf ellipticals and tidal stripping are rife (e.g. Muzzio et al. 1984; Bekki et al. 2003).

Thus in the major merger models, we would expect to see steeper radial color/metallicity gradients in galaxies with very rich GCS due to the relatively large number of blue GCs found at large galactocentric radius (Rhode & Zepf 2004).

One prediction of Beasley's model is that the formation of the red GCs will be extended over several Gyrs in low-density environments (Forbes et al. 2004). Semi-analytic models of galaxy formation predict that the largest spread in galaxy properties such as metallicity and age should occur for low luminosity early-type galaxies in under-dense environments.

Tonini (2013), using empirical galaxy mass-metallicity relation with observed galaxy stellar mass in the hierarchical model, predicts that the metal-rich sub-population should dominate GCS of galaxies in the field since they are expected to have evolved passively with little or no merger and interaction. Galaxies with prolonged star formation histories are also expected to have GCS dominated by red GCs. However, in galaxies with similar luminosities but more intense merger histories, the metal-poor clusters are expected to dominate. Fig. 3 summarize the predictions from Tonini (2013), where galaxies with poor merger histories e.g isolated ellipticals are expected to have GCS dominated by metal-rich GCs.

Results from the study of NGC 821, one of the few low density GCS studied (Spitler et al. 2008) gives the constraints on the GCS properties in an under-dense environment. All measured properties of its GCS indicate resemblance to similar-mass elliptical galaxies in higher density environments with its isolation producing no special discernable feature compared to ellipticals in cluster environments. Cho et al. (2012) studied ten low-luminosity ellipticals in low-density environments with the Advanced Camera for Surveys (ACS) on the Hubble Space Telescope and tentatively concluded that GCS in under-dense environments are either less metal-rich or younger (or both!) than those in high-density regions.

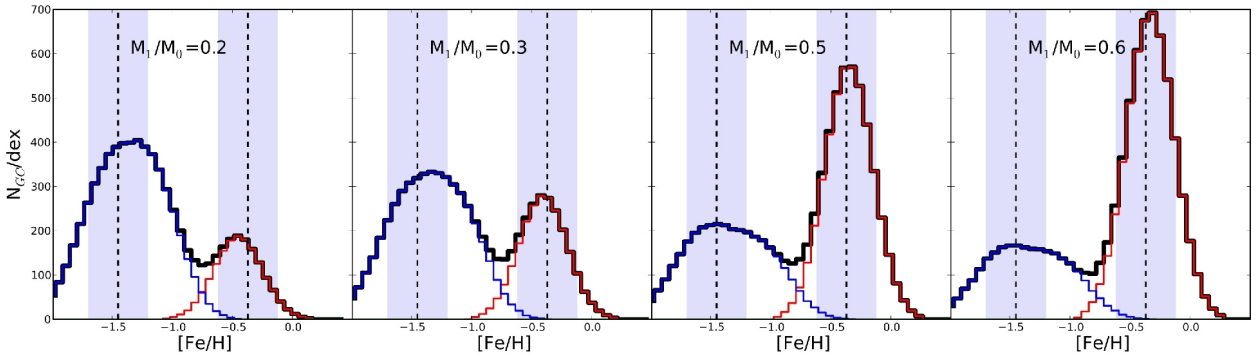

Figure 3: Variation of GC metallicity for galaxies with different assembly histories. Parameter M_1/M_0 is the ratio of stellar mass of the progenitor galaxy in the merger tree to the stellar mass of the galaxy at redshift z = 0. An isolated galaxy with more or less no merger or interaction should have the distribution in panel with $M_1/M_0 = 0.6$ (Tonini 2013).

1.5 Isolated Elliptical Galaxies

Elliptical galaxies are preferentially found in regions of high galactic density and low velocity dispersion, while spiral galaxies dominate in the field (Dressler 1980). This morphology-density relation implies that the probability of finding an early-type galaxy in a low density environment is low. Few ellipticals are thus found in the field and they are termed isolated ellitical galaxies. The hierarchical model suggests that isolated ellipticals are formed in the merger of many subclumps during the early stages of the evolution of the universe and are likely to show evidence of recent star formation and/or merger events. Gravitational interaction signatures like tidal tails, dust lanes and shells have been observed in some studies of isolated ellipticals by Reda et al. (2004); Tal et al. (2009); Lane et al. (2013).

Isolated elliptical galaxies could be formed from the collapse of poor groups of a few galaxies. Mergers at different redshifts of progenitors with different mass ratios and gas fractions are needed to reproduce these observed features. Niemi (2011) used the Millennium simulation to study the properties and formation history of isolated elliptical galaxies, and

compared their results with observational data. Despite the sparseness of the observational datasets available to them, they were able to conclude that isolated ellipticals are rare, with a small number of companions ranging from only a few dwarf companions to as much as about 20. Thus, isolated ellipticals are not completely without neighbours though by definition they are situated in low density environments.

1.6 Isolated Elliptical Galaxy Samples

Defining a "true" sample of isolated ellipticals is a complex task due to the presence of satellite galaxies and possible presence of dwarf galaxies around bright galaxies at the low end of the luminosity function. Samples of early-type galaxies in the field are found in literature with different isolation conditions (e.g. Karachentseva et al. 1986; Aars et al. 2001; Kuntschner et al. 2002; Stocke et al. 2004). For this study, we have made use of the isolated elliptical catalogs of Smith et al. (2004) and Reda et al. (2004).

Smith et al. (2004) made such a sample from galaxies in the Lyon-Meudon Extragalactic Database (LEDA)[1] by classifying as isolated ellipticals, galaxies that satisfied the following criteria:

- velocity of primary galaxy must be less than 10,000 km s^{-1}
- absolute magnitude of the galaxy must be brighter than $M_B \sim -19$
- galaxies must lie above a Galactic latitude of $|25°|$
- a de Vaucouleurs morphological type $T < -4$ from the LEDA database
- neighbours should be at least twice as faint as the primary candidate

The candidates were also visually confirmed as truly isolated before they were adopted.

[1]created in 1983 at Lyon Observatory, merged with Hypercat in 2000, now known as HyperLeda

Reda et al. (2004) also used LEDA as source catalogue but used a different set of criteria in defining their sample.

- morphological type $T \leq -3$
- Virgo corrected recession velocity $V \leq 9000$ km s^{-1}
- apparent magnitude $B \leq 14.0$
- galaxy not listed as a member of a Lyon Galaxy Group (Garcia 1993)
- no neighbours within 700 kms^{-1} in recession velocity, 0.67 Mpc in the plane of the sky and a magnitude of ± 2.0 in the $B-$ band of the primary galaxy

1.7 The Galaxy Sample

Our sample consist of three early-type galaxies imaged with the GMOS on the Gemini South telescopes. They are part of a larger sample of 5 isolated elliptical galaxies within a distance of 50 Mpc that are reachable from the southern hemisphere observed under Gemini programme GS-2012A-Q-6. Images of the Galaxy sample and basic data for the galaxies are presented in Fig. 4 and Table 1.1.

The William Herschel Deep Field (WHDF) (Metcalfe et al. 2001), taken from the Gemini Science Archive (GSA), is used to estimate background contamination from faint galaxies.

1.7.1 NGC 3962

NGC 3962 is classified as an E1 galaxy in the Crater constellation. It is an HI rich elliptical galaxy ($M_{HI} \sim 2.7 \times 10^9 M_\odot$ Serra & Oosterloo 2010) with two distinct kinematic subsystems (Buson et al. 1993; Zeilinger et al. 1996) with the outer arm-like feature thought to be

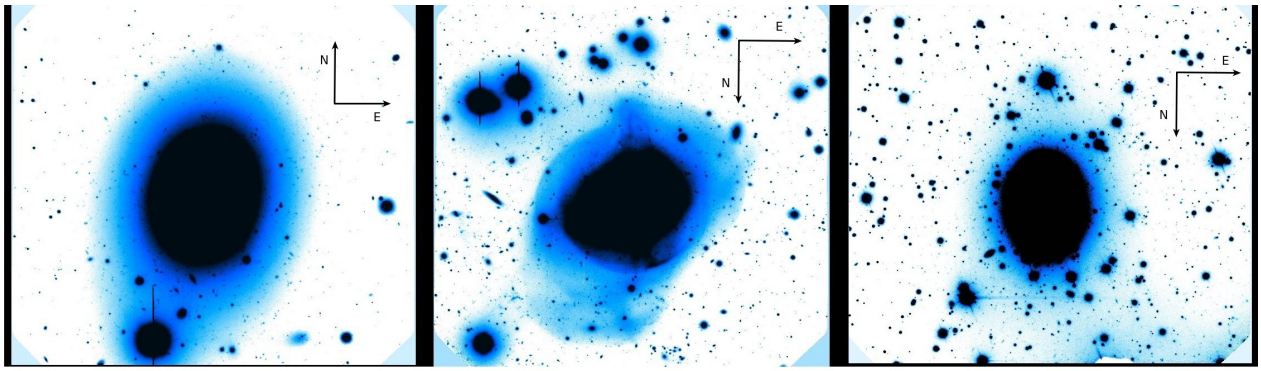

Figure 4: GMOS image of galaxies. NGC 3962 (left), NGC 2865 (center) and NGC 2271 (right). Each image has a FOV of $5.5' \times 5.5'$.

Table 1.1: Galaxy sample. Coordinates and distance are from NASA Extragalactic Database, B_T magnitudes from RC3 catalogue de Vaucouleurs et al. (1991), distance modulus from Tonry et al. (2001), extinction coefficient from Schlegel et al. (1998)

Galaxy	α_{J2000} (h:m:s)	δ_{J2000} (°:′:″)	l (°:′:″)	b (°:′:″)	B_T (mag)	M_B (mag)	$(m-M)_0$ (mag)	d (Mpc)	$E(B-V)$
NGC 3962	11:54:40.1	-13:58:30.0	282:39:10.8	-46:38:57.5	11.59	-21.15	32.74 ± 0.49	30.73	0.0452
NGC 2865	09:23:30.2	-23:04:41.0	252:57:10.8	+18:56:29.8	12.18	-20.71	32.89 ± 0.20	32.13	0.1182
NGC 2271	06:42:53.0	-23:28:34.0	233:13:30.0	-12:14:46.0	12.10	-20.41	32.51 ± 0.28	30.36	0.0841
WHDF	00:22:32.8	+00:21:07.5	107:34:49.5	-61:39:20.7					

associated with a bluer color component compared to the surrounding regions (Goudfrooij et al. 1994). The inner disk of NGC 3962 is rich in ionised gas - a signature of earlier merger with another galaxy. A young stellar population with age 2.5 ± 0.4 Gyrs is also hinted at by Serra & Oosterloo (2010). It is known to have a central radio source (Birkinshaw & Davies 1985). There is no report of any previous study of its GCS in literature.

1.7.2 NGC 2865

NGC 2865 is a classical shell galaxy in the Hydra constellation (Malin & Carter 1983) with abundant evidence of a recent minor merger or accretion that involves a gas-rich disc galaxy (see central panel in Fig. 4). It has a very luminous shell and an HI disk with ($M_{HI} \sim 5.3 \times 10^8 M_\odot$ Serra & Oosterloo 2010). The velocity profile has a clear signature of a

kinematically distinct core (KDC) in the central 4″ region (6.4 kpc) and solid-body rotation in the outer regions (Hau et al. 1999). Its chaotic shells are bluer than the main body of the galaxy and contributes $11 - 22$ % of the total luminosity (Fort et al. 1986). Hau et al. (1999); Serra & Oosterloo (2010) report the presence of a young stellar population with age $0.4 - 1.7$ and 1.1 Gyrs, respectively. Sikkema et al. (2006) in the study of the GCS of six shell galaxies reported the presence of a population of very blue, low luminosity GCs near $(V - I) = 0.7$ in the complex CMD of NGC 2865. This is evidence of the recent formation of GCs in the galaxy.

1.7.3 NGC 2271

NGC 2271 is classified as an E/S0 galaxy in the constellation Canis Major. NGC 2271 has a non-rotating kinematically decoupled central component within 1.5″ of the galaxy's center (Koprolin & Zeilinger 2000) which shows a disturbed structure (de Souza et al. 2004). Hau & Forbes (2006), however, could not confirm the presence of this distinct core and reported a smooth velocity profile and declining velocity dispersion. There is no report of any previous study of its GCS in the literature.

Chapter 2

Data and Reduction

2.1 Data

Raw images of the science targets were obtained using the GMOS[1] (Gemini Multi - Object Spectrograph) instrument in imaging mode on the 8.1 meter diameter Gemini South telescope in Cerro Páchon, Chile. The GMOS detector array consists of three 2048×4608 pixel CCDs with an unbinned scale of $0.0727''$ pixel^{-1}. A 2×2 on-chip binning was used such that pixel size is $0.146''$ pixel^{-1}. Binning increases S/N ratio, reduces final readout time and final image size. The FOV of the camera is $5.5' \times 5.5'$ with $2.8''$ (39 pixels) gaps between the chips. The instrument was used in the one-amp mode and dithered between exposures in the x-direction to facilitate removal of cosmic-rays, bad/hot pixels and the gaps between the CCD chips. Broad band imaging was done using SDSS[2] $g'(G0325)$ and $i'(G0327)$ filters. Table 2.1 contains details of observational parameters. It also includes the WHDF that we have used to estimate contamination from faint background galaxies in our FOV (see Sec. 2.8).

[1]Further information on GMOS can be found on the instrument homepage (`http://www.gemini.edu/sciops/instruments/gmos/`)

[2]Sloan Digital Sky Survey

Table 2.1: Summary of Observations. Table lists the date of observation, number of exposures taken with exposure times and seeing of co-added images in the two bands

Galaxy	Obs. date	Exp. time (s)		FWHM($''$)	
	(dd.mm.yyyy)	g'	i'	g'	i'
NGC 3962	22.02.2012	6×610	6×440	0.70	0.54
NGC 2865	25.01.2012	6×480	6×340	0.62	0.55
	26.01.2012	8×490[3]	6×350	0.56	0.48
NGC 2271	01.02.2012	9×419	9×315	0.70	0.62
WHDF	20.08.2001	6×300	6×300	0.86	0.67

2.2 Image reduction

The raw images obtained from GMOS were processed using the GEMINI GMOS package within IRAF [4](Image Reduction and Analysis Facility). Instrument signatures (overscan, gaps, bias)

were removed from the images using the GPREPARE, GIREDUCE and GMOSAIC task in IRAF. Appropriate bias and flat-field calibration frames in the g' and i' bands were obtained from the GSA.

GPREPARE was used to prepare raw GMOS images for reduction. GIREDUCE reduced the partly processed images in GMOS. It applied overscan correction by fitting and subtracting the overscan level and then trimmed the entire overscan section away by keeping only the section specified in parameter key_datasec. It also subtracted the bias image from the raw image and divided the image by the flat field image.

$$\text{final reduced object frame} = \frac{\text{raw object frame} - \text{bias frame}}{\text{normalized}\{\text{flat field frame} - \text{bias frame}\}} \tag{2.1}$$

Dark frames were not used in our calibration as the effect of dark currents is negligible.

[3]two of the exposures were not used as they have unusually poor seeing

[4]IRAF is distributed by the National Optical Astronomical Observatories, which are operated by the Association of Universities for Research in Astronomy, Inc., under cooperative agreement with the National Science Foundation

In the i' band (at longer wavelengths), there is significant fringing in GMOS images due to night sky emission lines. Full correction for fringing is very difficult due to its strong variability, hence we assumed that the shape of the fringe pattern is constant. GIRMFRINGE task removed fringing from GMOS images by subtracting the fringe frame. This was performed only on reduced images in the i' band.

GMOSAIC task was used to join the three GMOS CCDs images into one image. The resulting images for g' and i' (for each target) were then co-added separately using IMCOADD to remove the CCD gaps, cosmic-ray hits and bad/hot pixels from the final image. Using GEMSEEING task in GEMTOOLS package we determined images to be co-added. Images with very deviant FWHM values were not co-added. The FWHM from the observation log for the targets compares well with that of the final images in the g' and i' band from GEMSEEING, hence image quality is good.

Using X- and Y- windows with sizes of $7.88''$ and the MEDIAN task in IMFILTER package, we masked out as much of the galaxy light as possible without removing too many point sources in the final co-added images. IMARITH task which perfoms binary type arithmetic on images was used to do the actual galaxy light removal. These final co-added, galaxy-light subtracted images were then used for all the subsequent data analysis.

2.3 Object Detection and Photometry

At the distance of the science targets (see Table 1.1 in Chapter 1), most of the GCs would be unresolved (point sources). SExtractor (Bertin & Arnouts 1996) was used for object detection in the reduced images in both bands since it gives better result than DAOFIND task in IRAF for crowded extragalactic fields containing extended sources (DAOPHOT II manual). In crowded fields, neighbouring objects often overlap (centers are separated by distances significantly less than one FWHM), hence the need for accurate deblending before

any meaningful photometry can be done. SExtractor uses simple convolution kernels as simplifying approximations to deal with varying shapes and sizes of astrophysical objects, blending and variable point spread function (PSF) across the fields. It generates a catalogue of detected, deblended objects with flags, positions, fixed-aperture and adaptive-aperture magnitudes. Of special interest to this work is the CLASS_STAR parameter, also called stellarity index, used to distinguish between point sources and resolved sources. The neural network system of SExtractor assign detected sources CLASS_STAR parameter values from 0 to 1 with the limits corresponding to extended sources and point sources respectively. Objects can take values over the range.

The ideal configuration of SExtractor parameters should give as complete a sample as possible with accurate magnitudes i.e detect the faintest sources, perform deblending on overlapping objects in the crowded field without including false detections in the catalogue. We achieve this by performing sextraction using gaussian ($gauss\_4.0\_7 \times 7$) and mexican hat filters ($mexhat\_4.0\_9 \times 9$)[5] separately and combining the output into a single catalogue. The former uses a smaller aperture for its photometry, hence it returns more accurate magnitude than the later which gives a more complete sample by detecting faint objects and deblending objects more effectively. Duplicate entries in the final output catalogue were removed before photometry was done using the standalone DAOPHOT II and ALLSTAR (Stetson 1992).

The PHOT task within DAOPHOT uses a list of apertures defined in parameter file *photo.opt* to perform concentric aperture photometry on all the objects catalogued by SExtractor. A list of suitable point sources that are isolated from bright neighbours, not saturated and not too close to the edge of the frame is generated with the PICK task. This is used by the PSF task to generate a point spread function for the frame in a series of iterative steps. ALLSTAR, using parameters specified in *allstar.opt*, does multiple-simultaneous psf fitting of the photometric objects and writes output to $*.als$ file. Of particular importance to this

[5]naming convention for Sextractor filters is filtername_seeingFWHM(pixels)_filtersize(pixels)

Table 2.2: Aperture Correction

Galaxy	g'	i'
NGC 3962	-0.035 ± 0.008	-0.051 ± 0.064
NGC 2865	-0.034 ± 0.020	-0.020 ± 0.008
NGC 2271	-0.034 ± 0.003	-0.048 ± 0.022

work is the SHARP parameter, which together with the stellarity index from SExtractor is used to separate resolved objects from unresolved ones. SHARP for an object is linked to its intrinsic angular size, without any contribution from the atmosphere. For point sources, SHARP is close to zero; for resolved or blended sources, SHARP is significantly more than zero while for cosmic rays and bad pixels, SHARP is significantly less than zero. The detected objects in the g' and i' frames were matched using their positions with DAOMATCH and DAOMASTER, thus we obtained colors for all photometrically detected objects.

2.4 Photometric Calibrations

We made corrections for the finite size of apertures used in obtaining the psf magnitudes by applying the magnitude difference between the 15 pixel (outermost concentric radius used in $*.opt$ parameter file) and 25 pixel (outer sky annulus radius in $*.opt$ parameter file) radii apertures to the psf magnitudes for all of the detected objects. Summary of the aperture corrections (in magnitudes) can be found in Table 2.2. We accounted for foreground galactic extinction in the science targets using values from Schlegel et al. (1998)[6], extinction ratios $A_g = 3.793E(B-V)$ and $A_i = 2.086E(B-V)$. We then added a factor of $2.5 \times \log_{10}$(EXPOSURE TIME) to the total magnitude to obtain extinction-corrected instrumental magnitudes. To convert the instrumental magnitudes to standard SDSS magnitudes, we used images of standard star fields taken during nights when the science targets were observed in the g' and i' bands. The images were reduced the same way as the science frames but

[6] `http://irsa.ipac.caltech.edu/applications/DUST/`

without performing GIRMFRINGE since exposure times were significantly shorter. For each of the reduced standard star frames, we created a catalog of the magnitudes and color indices of the standard stars on the standard system using a combination of PHOTCAL in IRAF, SKYCAT and zero-point magnitudes from the Southern $u'g'r'i'z'$ standard star catalog[7] from Smith et al. (2002). We obtained the following transformation equations:

$$g' - i' = \frac{G' - I' - Z_{pg} + Z_{pi} - k_g(X_g - 1.0) + k_i(X_i - 1.0)}{1.0 + CT_g - CT_i} \tag{2.2}$$

$$i' = I' - Z_{pi} - CT_i(g' - i') - k_i(X_i - 1.0) \tag{2.3}$$

where G' and I' are the instrumental magnitudes; Z_{pg} and Z_{pi} are the zero-point magnitudes for g' and i' bands respectively; k_g and k_i are the atmospheric extinction coefficients in g' and i' bands respectively; X_g and X_i are airmasses in g' and i' bands respectively.; CT_g and CT_i are color terms in the g' and i' bands respectively at Cerro Páchon, with values corresponding to each science target in Table 2.3. We have used the color term values obtained for NGC 2865 for all our science targets due to the small number of standard stars available for the others. In the transformations, we accounted for atmospheric extinction due to location of observatory and altitude of science targets and made corrections for color term due to variations in throughput of the telescope's optical system as a function of wavelength.

2.5 Completeness Test

We performed completeness test on all the galaxy-light subtracted frames to determine the magnitude limits of our observations with both filters on all science targets. Using ADDSTAR task in DAOPHOT II, we added 3000 artificial stars to each frame in a series of 10 independent experiments, placing the stars at random positions (300 at a time to avoid overcrowding the images). We repeated this for 5 different seeds, thus adding a total of 15000 artificial stars

[7] `http://www-star.fnal.gov/Southern_ugriz/New/index.html`

Table 2.3: Photometric calibration using standard stars from the Southern standard star catalog

Galaxy	Zero Point mag		Color term		rms		no. of stars	
	g'	i'	g'	i'	g'	i'	g'	i'
NGC 3962	-3.110 ± 0.034	-2.770 ± 0.033	-0.055	-0.024	0.101	0.103	9	11
NGC 2865	-3.253 ± 0.022	-2.917 ± 0.012	-0.055	-0.024	0.046	0.041	16	14
NGC 2271	-3.226 ± 0.005	-2.900 ± 0.007	-0.055	-0.024	0.035	0.028	11	11

per frame. The stars were created using corresponding point spread functions earlier obtained and added over magnitude range of $19.5 < M_{object} < 28.0$ where most GCs lie. The new frames are analysed exactly the same way as the original images. We made plots of fraction of added stars recovered against magnitude and fit with a Pritchet function (Fleming et al. 1995) using Markwardt IDL curve fitting library (Markwardt 2009). Pritchet function is given by :

$$f = \frac{1}{2}\left[1 - \frac{\alpha(m - m_{lim})}{\sqrt{1 + \alpha^2(m - m_{lim})^2}}\right] \tag{2.4}$$

where m_{lim} is the magnitude at which the recovered fraction, $f = 0.5$ and α controls how quickly f declines (the larger the value of α, the steeper the transformation from 1 to 0). From Table 2.4 and Fig. 5, the completeness magnitudes in i' fall faster than in g'. Based on the completeness test, the detection is 80% complete at $i' = 25.1$, 25.8 and 24.6 for NGC 3962, NGC 2865 and NGC 2271 respectively.

2.6 Object Classification

The detected objects consist of GCs, foreground stars and faint background galaxies - unresolved and resolved sources. Artificial star experiment enable us characterize the true behaviour of the CLASS_STAR and SHARP parameters of point sources in our fields by defining their boundaries in order to classify detected sources as resolved or unresolved. To

Table 2.4: Completeness Parameters

Galaxy	g'		i'	
	[8]m_{lim}	α	m_{lim}	α
NGC 3962	26.70	2.06	25.40	3.04
NGC 2865	27.31	1.90	26.24	2.95
NGC 2271	26.20	1.32	25.40	1.63

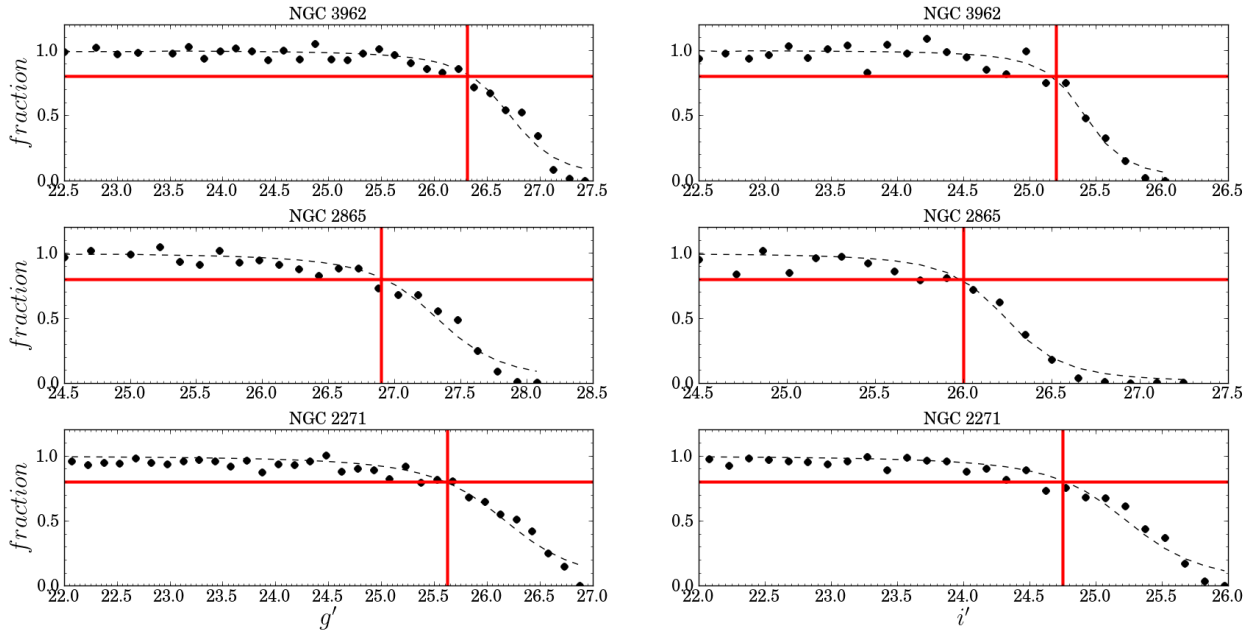

Figure 5: Fraction recovered in artificial star experiment. The dots are the fraction of artificial stars recovered as a function of magnitude. The dashed lines are the fitted Pritchet function. The vertical red lines indicate magnitudes where the detection is 80% complete.

classify the detected objects, we made plots of the CLASS_STAR and SHARP parameters for the recovered artificial stars against aperture magnitudes with overplots of these parameters for the science fields.

[8]magnitudes quoted here are at 50% completeness

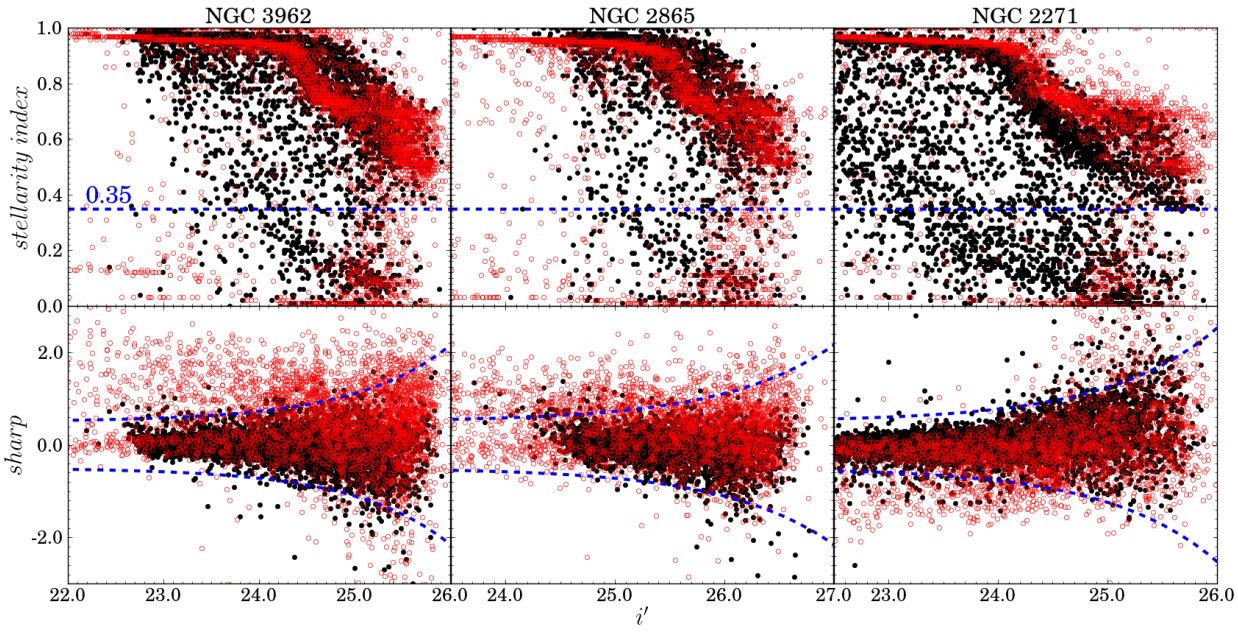

Figure 6: Upper panels contains plot of stellarity index vs aperture magnitude for detected, artificially added stars (open red circles) and all detected sources in our science targets (black filled circles). Objects with stellarity index more than 0.35, the blue dashed line, are unresolved point sources. Lower panel is the plot of sharp parameter vs aperture magnitude with red and black markers same as above. Objects with sharp parameters between the blue dashed lines are unresolved point sources.

We define unresolved objects in the science fields as those with CLASS_STAR and SHARP parameters in the region defined by the recovered artificial stars. Fig. 6 contains plots of stellarity index and sharp parameters for detected artificial stars (blue circles) and science objects (green circles) in the i' field. Objects with CLASS_STAR > 0.35 and with SHARP values within range in equations 2.5, 2.6 and 2.7 are classified as unresolved.

$$\text{NGC} \quad 3962 : \begin{cases} -0.5 - \exp(i' - 25.5) \leq \text{SHARP} \leq 0.5 - \exp(i' - 25.5) & i' \\ -0.5 - \exp(g' - 26.4) \leq \text{SHARP} \leq 0.5 - \exp(g' - 26.4) & g' \end{cases} \tag{2.5}$$

$$\text{NGC} \quad 2865 : \begin{cases} -0.5 - \exp(i' - 26.5) \leq \text{SHARP} \leq 0.5 - \exp(i' - 26.5) & i' \\ -0.5 - \exp(g' - 27.5) \leq \text{SHARP} \leq 0.5 - \exp(g' - 27.5) & g' \end{cases} \tag{2.6}$$

$$\text{NGC} \quad 2271 : \begin{cases} -0.5 - \exp(i' - 25.5) \leq \text{SHARP} \leq 0.5 - \exp(i' - 25.5) & i' \\ -0.5 - \exp(g' - 27.5) \leq \text{SHARP} \leq 0.5 - \exp(g' - 27.5) & g' \end{cases} \tag{2.7}$$

2.7 Globular cluster candidate selection

To obtain a clean sample of GC candidates, we used the 80% completeness values in i' magnitude to define the faint magnitude limits. This is because we have better seeing in i' band (see Table 2.1). To define the bright magnitude limit for each frame (in i'), we used the integrated magnitude of ω Cen, the most massive galactic GC-like object, with an integrated magnitude of $M_I \sim 11.5$ and distance moduli from Table 1.1. Based on previous GC studies using g' and i' filters (Forbes et al. 2004; Wehner et al. 2008; Faifer et al. 2011), we applied a reasonable color cut of $0.4 < g' - i' < 1.4$ and the previously obtained magnitude limits to our sample of detected objects to obtain our GC candidates.

2.8 Contamination from Background Galaxies

Contamination from background galaxies and foreground stars is inevitable in deep photometric studies of extragalactic objects. Contributions to the contamination from faint unresolved background galaxies dominate in the faint magnitude regime where they appear more extended than GCs. This contamination can be statistically estimated and appropriate corrections can be applied to photometric results. To do this, we used the g' and i' WHDF

Table 2.5: Background Galaxy Contamination

Galaxy	GC Candidate	Contamination
NGC 3962	719	43
NGC 2865	602	132
NGC 2271	435	15

images obtained from the GSA. We applied the same routines we used for our science targets to detect objects, perform photometry, calibrate, test for completeness and classify detected objects in the comparison fields. We ensured that our comparisons were done over similar magnitude range by using the 80% completeness faint magnitude limits from our science targets. The number of unresolved objects obtained in the WHDF analysis is taken as statistical estimate of the background contamination.

WHDF photometry was not deep enough compared to that of NGC 2865, thus the need for a workaround solution. We extrapolated the Pritchet function for WHDF to the 80% i' magnitude limit for NGC 2865 and assumed that α would remain constant. We then numerically integrated Pritchet function over 10 magnitude bins from $i'_0 = 25.58$ to $i'_{fin} = 25.80$ to determine fraction of objects that would have been detected if our photometry was that deep. For each extrapolated WHDF magnitude bin, the number of WHDF objects is the product of the number of objects in NGC 2865 magnitude bin and the ratio of the integral to the area of the bin. We thus get an extra 69 background contaminants whose color values we randomly generated from the color sample for WHDF.

A summary of the GC candidates and statistically obtained background contamination is given in Table 2.5. NGC 2865, with the deepest photometry, has more background galaxy contamination. Even though NGC 3962 is at a higher galactic latitude compared to NGC 2271, it has a higher contamination level due to its deeper photometry.

Chapter 3

Results

CMDs for all detected sources (resolved and unresolved) in the GMOS fields studied are presented in Fig. 7 with all detected objects that fall into the color and magnitude ranges defined for GC candidates in Section 2.6 represented as red-filled circles, unresolved and resolved objects that are not GCs are represented by the big black-filled and small circles respectively. Very easily, apart from NGC 2865, the GC candidate population is seen as the dominant collection of points around $(g' - i') \sim 0.9$ and color bimodality is evident only in NGC 2271 at bright GC magnitudes. In all GCS studied, field contamination and photometric scatter is stronger at fainter magnitudes. In the faint magnitude regimes, contamination is dominated by unresolved background galaxies and in the brighter magnitudes, by MW stars.

NGC 3962 has some bright, unresolved sources with GC-like color but with i' magnitudes brighter than in GCs (see left panel of Fig. 8). These objects are ultra-compact dwarf (UCD) candidates. UCDs, first discovered by Hilker et al. (1999) in galaxy clusters, have sizes of 10 pc $<$ $\mathrm{r_{half}}$ $<$ 100 pc and typical luminosity of $L \sim 10^7 L\odot$. Their formation mechanism, however, is unclear. They could be formed from the stripping down of the nuclei of dwarf ellipticals in dense environments (Bekki et al. 2001), or from star cluster mergers (Kroupa 1998) or produced by changes in the physics of cluster formation when mass is high (Murray 2009). Hau et al. (2009) however suggests that mode of UCD formation should be independent of environment. Till date, no UCD has been found in any isolated elliptical galaxy.

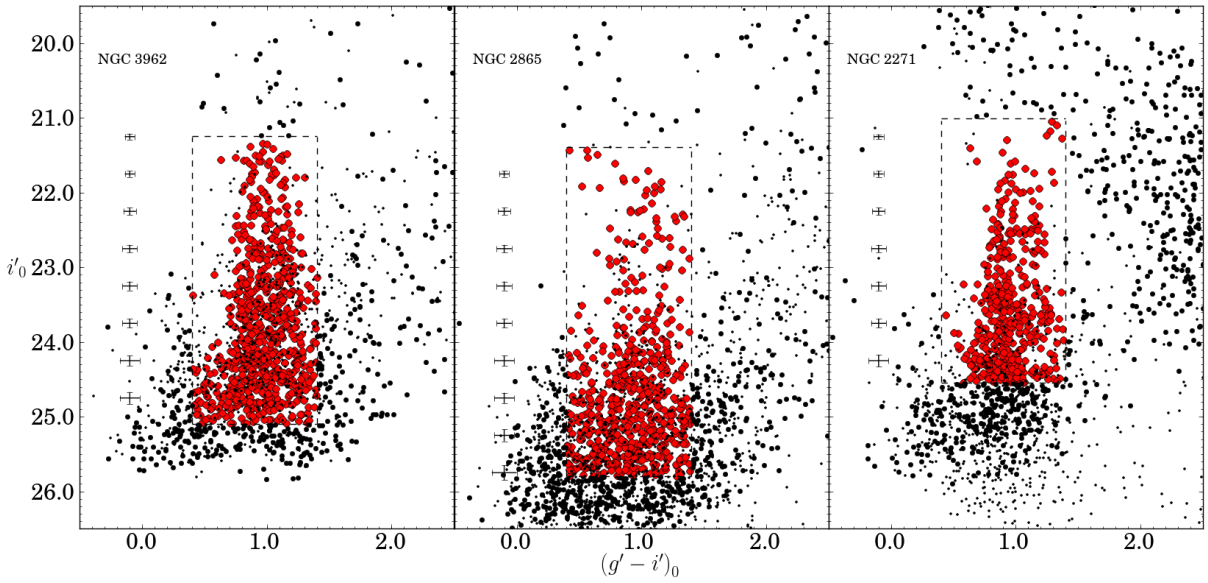

Figure 7: Color-magnitude diagrams of all detected objects in the FOV of the isolated elliptical galaxies. Photometric errors at different magnitudes are shown on the left. The dashed lines represent the limits we have defined for GC candidates. The red filled circles are the GC candidates

In the right panel of Fig.8, the unresolved UCD candidates are marked on the GMOS image of NGC 3962 as green triangles while the diamonds are resolved objects with parameters in the UCD range. Visual inspection confirms that these objects are evenly distributed spatially along the semi-major axis of the galaxy, close to the central regions. Further spectroscopic studies to confirm their UCD status is ongoing using data obtained in April, 2013 from the Nordic Optical Telescopes, La Palma. Also, from the CMD of NGC 3962, there is a small subgroup of faint, blue GC candidates which could be wrongly classified faint background galaxies or blue stars.

The CMD of detected sources in NGC 2865 (see central panel of Fig. 7), a shell galaxy with obvious signs of recent minor merger (e.g Sikkema et al. 2006; Hau & Forbes 2006), shows no clearly distinct color peak. There seems to be a group of blue GCs with average color ~ 0.6, distinct from the main GC distribution.

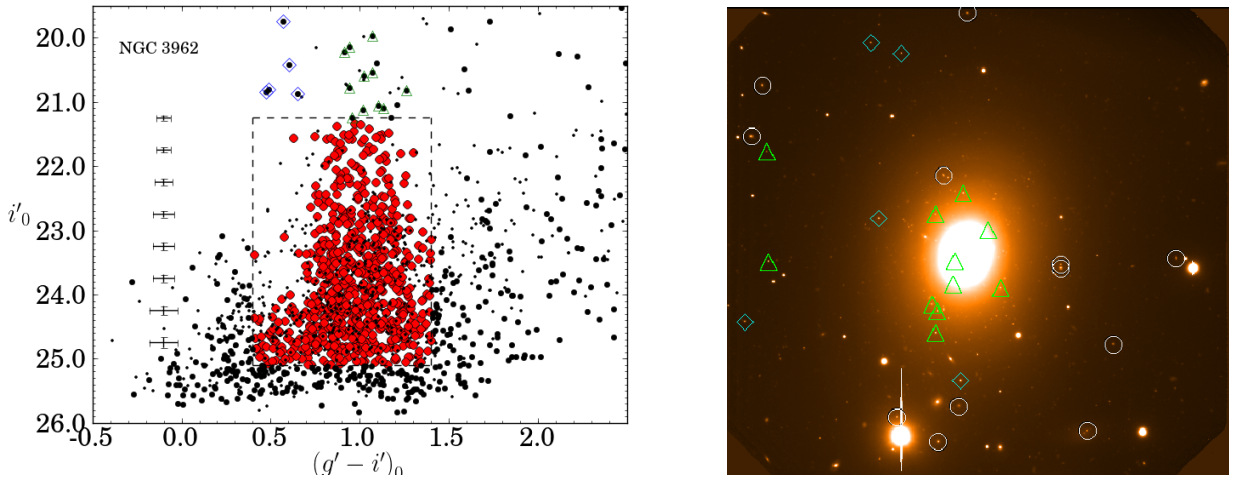

Figure 8: In the left panel, UCD candidates are marked with green triangles and blue diamonds on the CMD of NGC 3962. In the right panel, the UCD candidates are marked with green triangles and cyan diamonds. Note the axial distribution of the UCD candidates

3.1 Color distribution of globular clusters

This section describes quantitatively the color distribution of our GCS using statistical tools. We generated statistically-cleaned samples of GC candidates for each GCS and obtained $(g' - i')$ color distributions. Using B_{opt} , the "optimal" bin size from Izenman (1991) with $B_{opt} = 2IQRn^{-1/3}$, where IQR is the interquartile range of the ranked colors and n the sample size, we grouped the GC candidates and faint galaxy contaminants into color bins and randomly determined what objects to "clean" out per bin. The contamination removal was done randomly since we only know the number of contaminants to remove per bin and not the colors. We performed the iterations 100 times for each GCS and determined the number of Gaussian distributions in each output set using the Gaussian Mixture Modelling (GMM) algorithm (Muratov & Gnedin 2010). In Fig. 9, we plot the distribution of raw color peaks and dispersion for NGC 3962 for all iteration steps and see that sample distribution can be described by Gaussian functions. Thus we use average color peaks and dispersion for

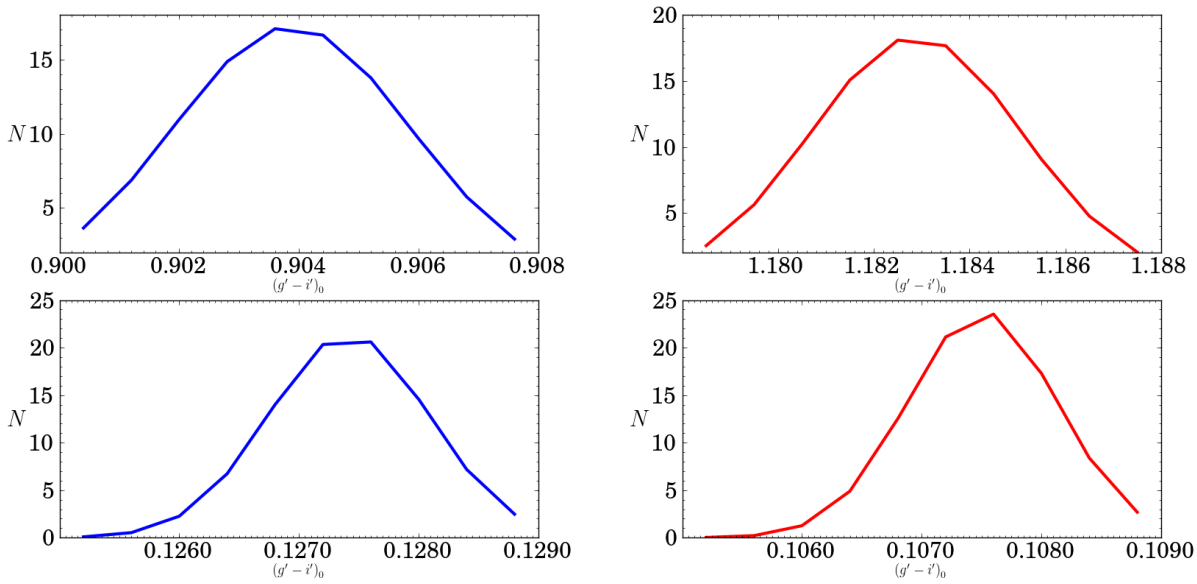

Figure 9: Top panels contain distribution of blue and red peaks returned by GMM per 100 iterations while lower panels contain distribution of dispersions.

subsequent analysis.

GMM uses expectation-maximization (by comparing the likelihood ratio test (LRT) of a sample having a unimodal distribution to a multimodal one) to identify the number of Gaussian distributions in a dataset based on some initial user defined guess for peak values and dispersions. It works on the assumption that the distributions are Gaussian, allowing for both homoscedastic (same dispersion) and heteroscedastic (different dispersion) fits unlike other distribution fitting algorithms like RMIX[1] which offers flexibility in the functional form of the curve. GMM performs independent tests of bimodality, unlike KMM Ashman et al. (1994) and RMIX, using the LRT, peak separation (D) and kurtosis (K) parameters from the input dataset to determine if a unimodal description can be rejected in favor of a multimodal one if the three statistics have sufficiently low values with $D > 2$ and $K < 0$. GMM also calculates the probability of each data point belonging to a particular mode.

[1] `http://www.math.mcmaster.ca/peter/mix/mix.html`

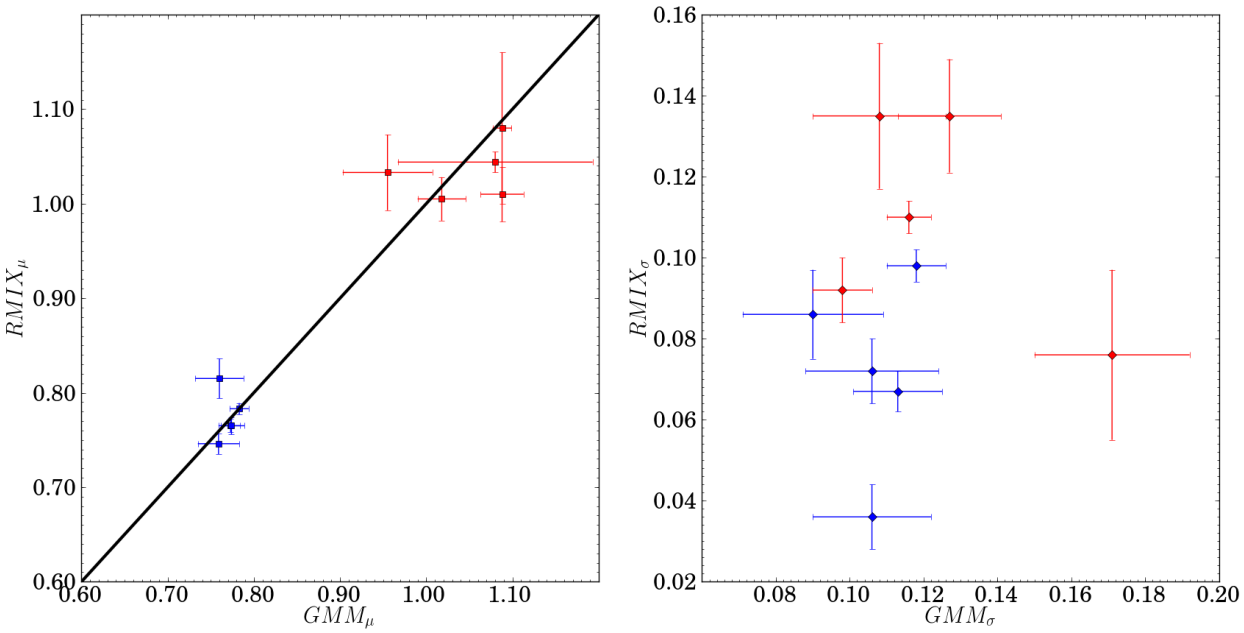

Figure 10: Left panel compares μ_{blue} and μ_{red} returned by RMIX with GMM while right compares dispersions

Galaxy	μ_b	σ_b	μ_r	σ_r	f_r	K	D
NGC 3962	0.89 ± 0.03	0.11 ± 0.01	1.15 ± 0.05	0.12 ± 0.02	0.30 ± 0.11	-0.05	2.21 ± 0.23
NGC 2865	0.92 ± 0.08	0.16 ± 0.03	1.24 ± 0.06	0.09 ± 0.03	0.27 ± 0.12	-0.62	2.96 ± 0.49
NGC 2271	0.90 ± 0.01	0.14 ± 0.01	1.22 ± 0.02	0.08 ± 0.01	0.16 ± 0.04	-0.34	2.84 ± 0.23

Table 3.1: GMM fits to the $(g' - i')$ color distribution. Col. 1: system name; Cols. 2 and 3:mean value and dispersion of blue sub-population; Cols. 4 and 5: mean value and dispersion of red sub-population; Col. 6: fraction of GCs assigned by GMM to the red sub-population; Col. 7: kurtosis of color distribution; Col. 8: peak separation, D=$\mid \mu_{\rm blue} - \mu_{\rm red} \mid /[(\sigma^2_{\rm blue} + \sigma^2_{\rm red})/2]^{1/2}$

To see if GMM and RMIX give consistent results, we generated color peaks and dispersions for the five galaxies in the dataset of Faifer et al. (2011) using GMM and compare results from RMIX and GMM and see that both give similar results for the same dataset (see left panel of Fig. 10) with clear one to one relationship between the color peaks. Dispersion is however not well behaved (right panel of Fig. 10 b), hence we use only color peaks for subsequent analysis. The means and dispersions of the best fitting Gaussian for sub-populations detected in all GCS are presented in Table 3.1.

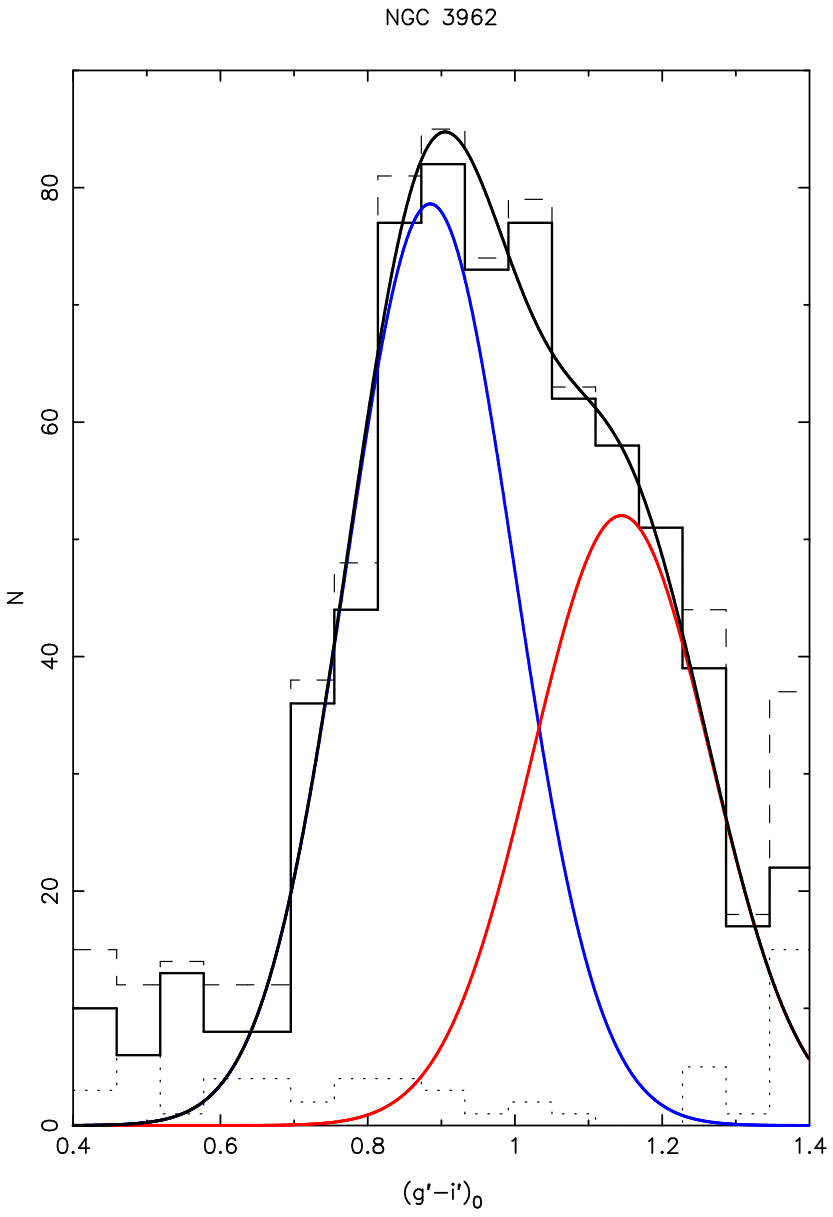

Figure 11: Histogram with overplot of best fitting Gaussians from GMM. Blue and red solid are individual Gaussians while black curve is their sum. The dashed, solid and dotted histograms represents raw, corrected and contamination data respectively

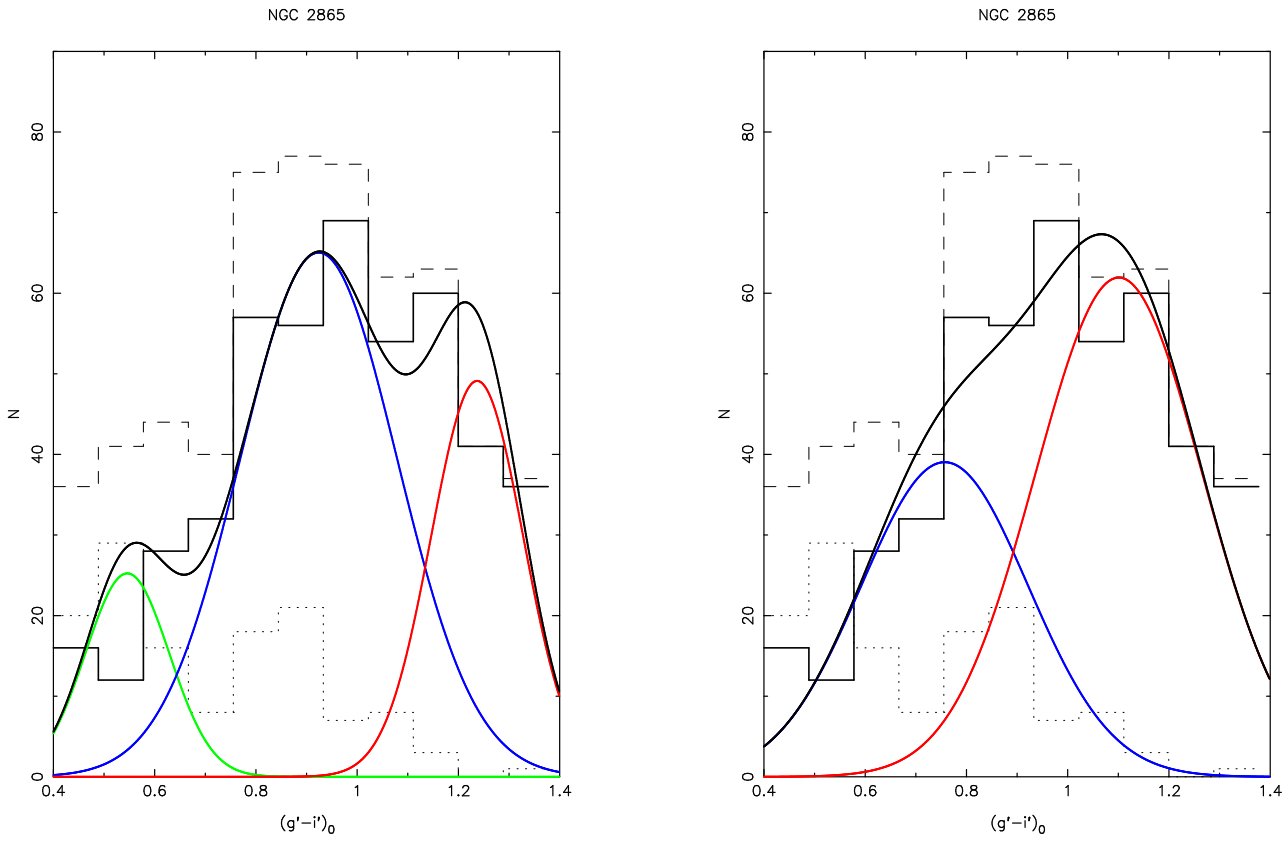

Figure 12: Histograms describing GCs detected in NGC 2865 by three- and two-Gaussian fit from GMM. Green Gaussian in first plot represent very blue sub-population. Blue and red solid are individual Gaussians while black curve is the sum of the Gaussians. The dashed, solid and dotted histograms represents raw, corrected and contamination data respectively

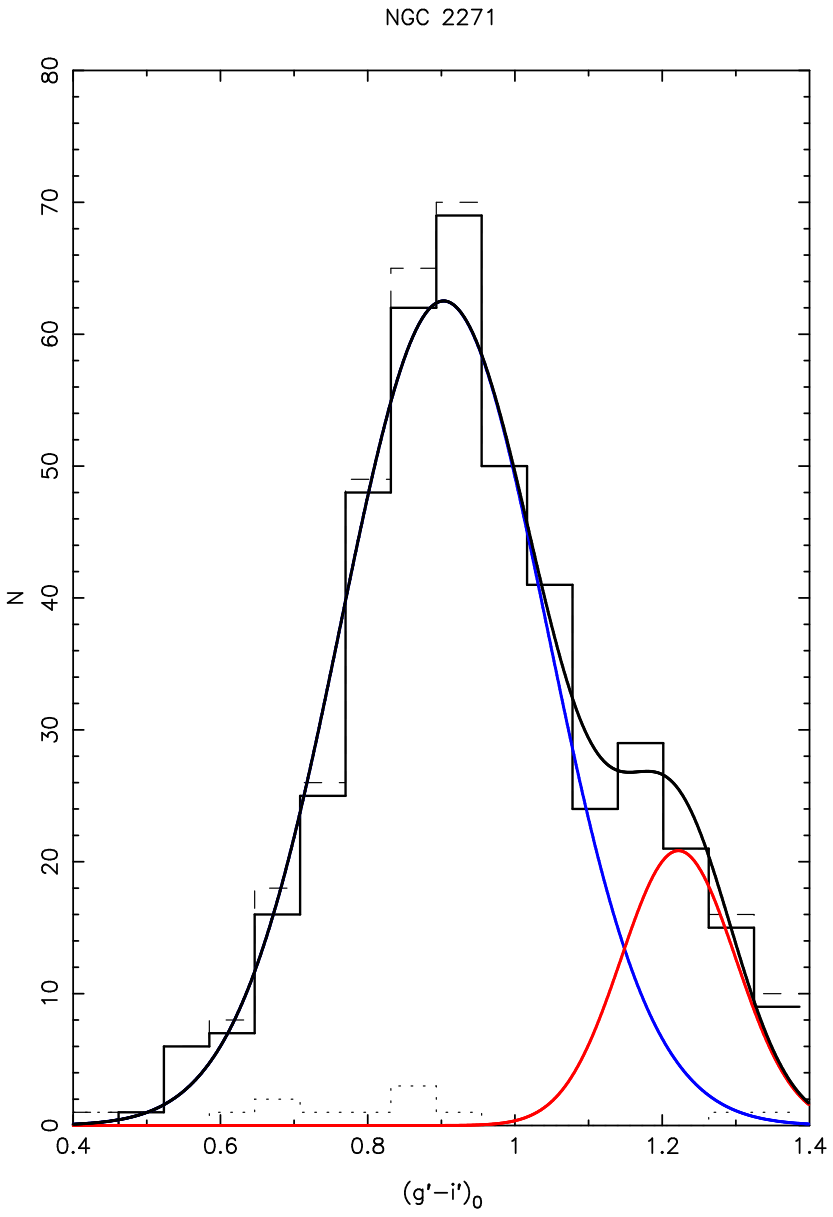

Figure 13: Histogram with overplot of best fitting Gaussians from GMM. Blue and red solid are individual Gaussians while black curve is their sum. The dashed, solid and dotted histograms represents raw, corrected and contamination data respectively

Fig. 11,12,13 show overplots of best fitting Gaussians (blue and red Gaussian curves) on $(g' - i')$ color distributions of GC samples before "cleaning" (dashed histogram), after statistically correcting for background galaxies (solid histogram) and that of the contamination (dotted histogram). The black curve is the sum of the Gaussians for the blue and red GC sub-populations.

Color distribution for NGC 2865 can be described by a three-Gaussian heteroscedastic model[2] with the bluest sub-population having a mean color of $(g' - i') = 0.53$. This translates to $V - I = 0.74$ if we use UBVRI to SDSS transformation equation from Usher et al. (2012), thus confirming the very blue, low luminosity population with average color of $V - I = 0.7$ detected by Sikkema et al. (2006) though they could not obtain good fits to the modes. Comparing the χ^2 from GMMs output for both models in the case of NGC 2865 and testing against the null hypothesis that a unimodal best describes our GC sample, the probability that a heteroscedastic, three-Gaussian description of our sample is due to chance is lower than that of a homoscedastic, two-Gaussian model, hence it is strongly preferred. This further supports the claim that NGC 2865 has a very blue, metal-poor, low luminosity and young subgroup (Hau et al. 1999). A sufficiently deep wide field photometric study of this GCS would help to obtain a more definite result.

3.2 Radial distribution of globular clusters

We used the probability returned by GMM to classify our GC candidates into sub-populations, unlike the "color-valley" approach commonly used in literature (e.g Faifer et al. 2011) and made plots of the spatial distributions of the blue and red sub-populations for each GCS (see Fig. 14).

As expected (e.g Geisler et al. 1996), the metal-poor subgroups have a more extended

[2]NGC 2865 can also be described by a two-Gaussian homoscedastic model

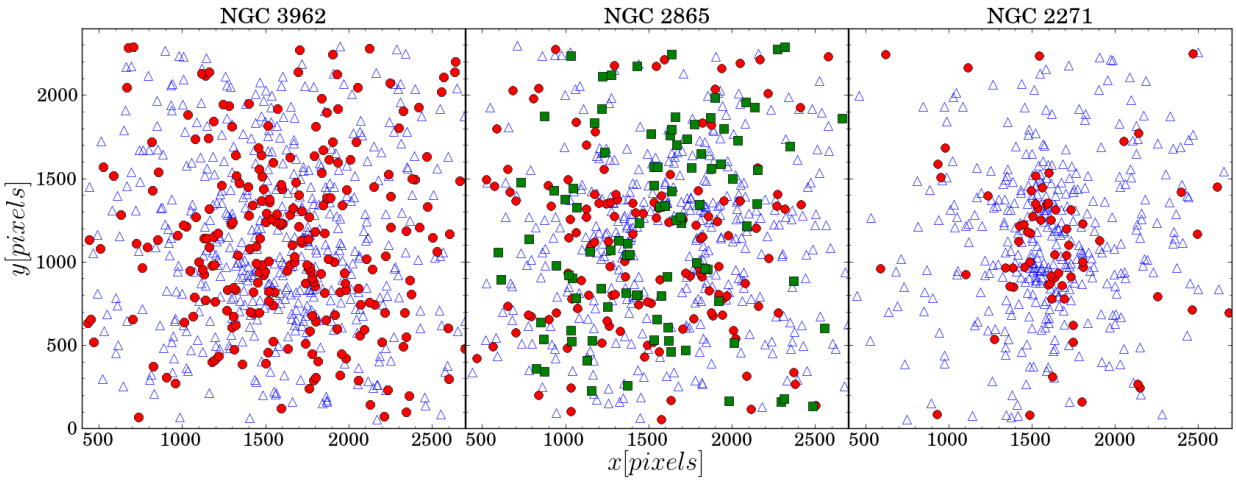

Figure 14: Spatial distribution (pixels) of detected GC candidates in GMOS FOV for galaxy sample. Blue triangles, red circles and green squares (only for NGC 2865) are the blue, red and very blue, young population detected

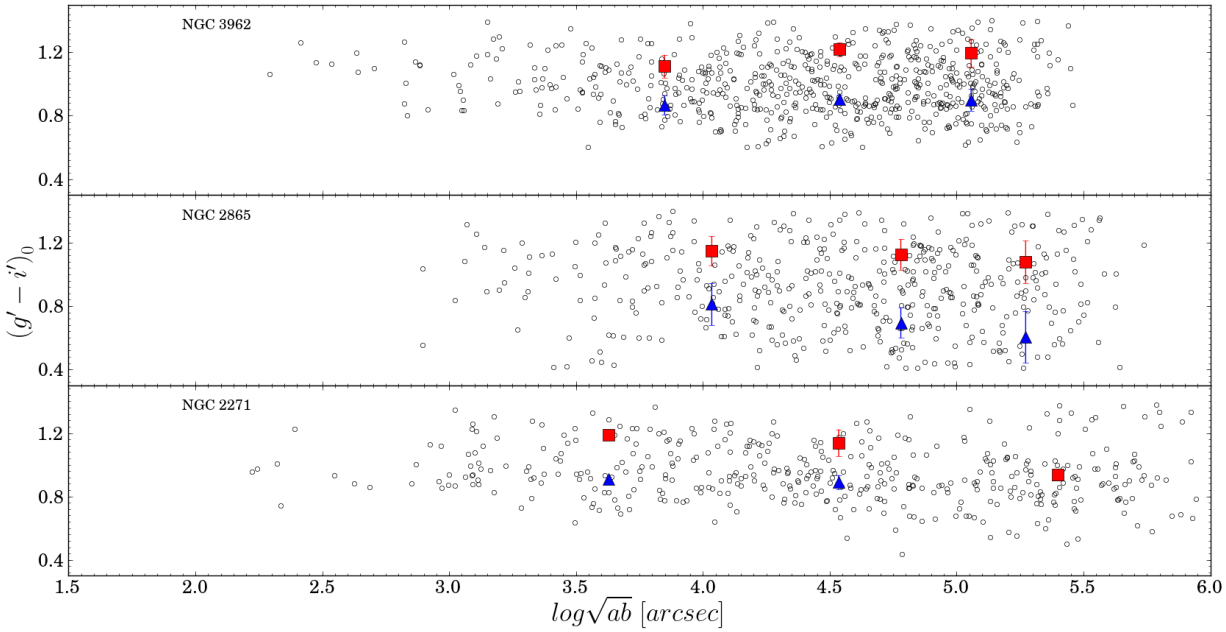

Figure 15: Plots of $(g' - i')$ color of detected GCs against radial distance (arcsec) with overplots of peak blue and red sub-population colors for radial bins containing equal number of objects

distribution and the metal-rich subgroups are relatively more centrally concentrated. For NGC 2865, we have included (green markers) the very blue subgroup. The gap in the center

of the plot corresponds to the region we lost to the bright, saturated galactic center in our photometry.

Each GCS sample was further divided into three (to have sufficient number of points to analyse with GMM) radial bins containing approximately the same number of GCs and we determined the average color, blue and red peaks for each bin. Using eccentricity and position angle data of our galaxies from NED[3] we derived the radial distance of each GC candidate from the galaxy center. We made plots of the color peaks within each bin against the projected radial distance (in units of $\log\sqrt{ab}$) with overplots of the GC candidate radial distribution in Fig. 15. We studied how the average color varies with galactocentric distance (see Fig. 16) by binning GCs into groups with variable sizes but with equal number of clusters and determined the color gradients by fitting with error-weighted, chi-square minimized straight lines of the form

$$(g' - i') = slope \times \log\sqrt{ab} + intercept$$

All the studied GCS have shallow negative gradients with average GCS color becoming bluer as we move away from galaxy center. NGC 2271, the most extended GCS and least luminous galaxy in our study, has the steepest gradient of -0.041 ± 0.015. NGC 3962 and NGC 2865 have gradients of -0.015 ± 0.016 and -0.029 ± 0.024 respectively. The very steep color gradient of NGC 2271 is due to the drop in the number of red clusters as we move away from the center of the galaxy. However, due to the relatively small number of GCs detected we could not perform this analysis on the sub-populations. Also, it would be instructive to note that due to the limited FOV of GMOS ($5.5' \times 5.5'$), these gradients are best representative of the "inner halo" GCs. A wide field photometric study would help characterise any transition in gradients in the outer regions and test the two-phase model for formation of

[3] *ned.ipac.caltec.edu*

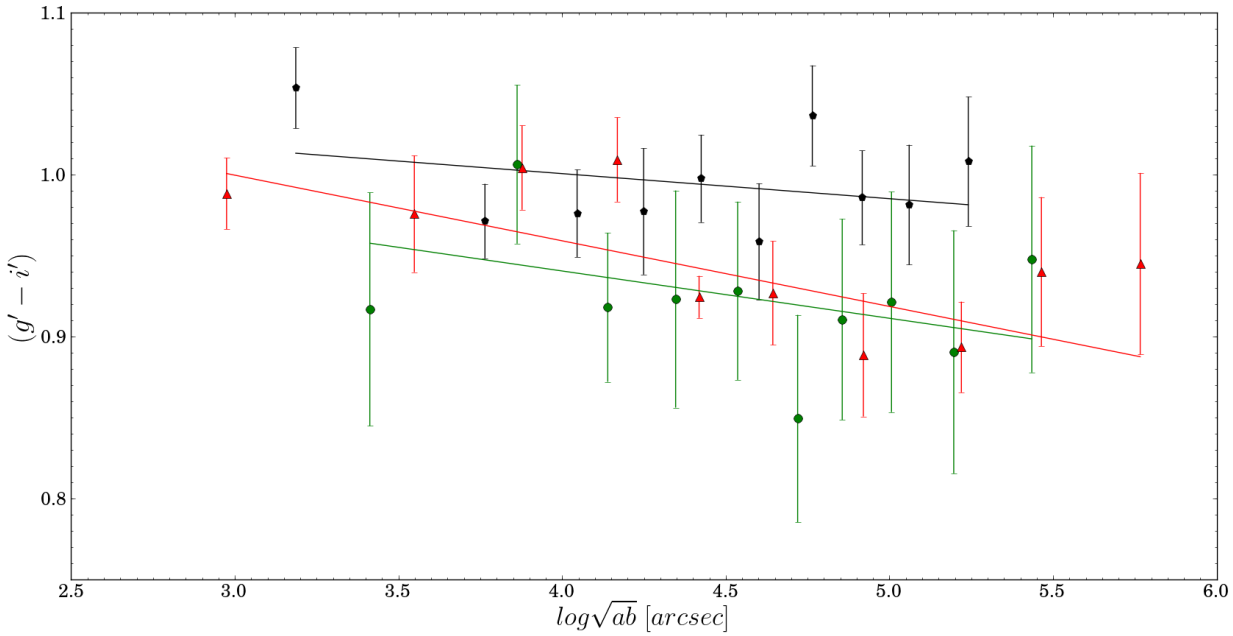

Figure 16: Variation of average $(g' - i')$ color in detected GCs with galactocentric distance (arcsec). Straights lines are fits to the data with black hexagons, green circles and red triangles representing NGC 3962, NGC 2865 and NGC 2271 respectively

elliptical galaxies since color gradients are due to rapid dissipational collapse (e.g Oser et al. 2010) and flattened in mergers (Di Matteo et al. 2009).

Chapter 4

Discussion

4.1 Host galaxy properties versus globular cluster properties

We compare GC properties obtained for our sample with host galaxy properties in different environments. The properties of interest are peak colors of sub-populations, average colors of detected GCs, peak separation in GCS and fraction of GCS that is metal rich and we study how they vary with host galaxy luminosities and the local density of galaxies.

The peak color of the red sub-population as well as the average color are known to show strong correlation with host galaxy luminosity (e.g Larsen & Richtler 2000). Also, the peak separation is a measure of how well we can describe the GCS as multimodal (Wehner et al. 2008) and we seek to characterise this parameter as a function of the host galaxy and its local environment.

Different models predict dominance by different sub-population e.g in Tonini (2013), the red sub-population is expected to dominate the GCS whereas in the multiphase collapse model,the metal-poor subgroup should be more dominant. We compare red fractions of the GCS at different luminosities and from different environments. Galaxy luminosity is a proxy for stellar mass, hence more luminous galaxies (more massive halos) are expected to be more efficient at retaining and mixing metals during the epoch of GC formation (Liu et al. 2011).

The local density of galaxies is a crude approximation of its isolation. Though biased

towards high luminosity isolated ellipticals, it provides a common quantitative basis for comparing GC properties in distant systems and nearby ones. For this study, we have adopted values from the Nearby Galaxies Catalog of Tully (1988) where local density ρ, in units of galaxies/Mpc^3, is defined only for galaxies brighter than -16 mag (blue apparent magnitude corrected for reddening) and velocity (corrected for local motion) less than 3000 kms^{-1}. The values were obtained using a 3D grid with 0.5 Mpc spacing. For NGC 2271, we use the local density of NGC 2227, the nearest galaxy to NGC 2271 in the catalog, at a distance of 27.5 Mpc since the catalog contains no data for NGC 2271.

We compare our result with studies of GCS in both dense and low-density environments using the works of Peng et al. (2006) and Cho et al. (2012). Peng et al. (2006) studied the color distributions of GCS in 100 elliptical galaxies in the dense Virgo cluster environment over a dynamic luminosity range with ACS using g and z filters. For this study, we include only galaxies with magnitudes with $-20.33 \leq M_B \leq -18.50$ so as to minimize any galaxy luminosity dependence. Peng et al. (2006) generally found a bimodal color distribution in all galaxies studied and observed that mean GC color increased with galaxy luminosity. For fraction of GCs detected that belong to the red sub-population, we use Peng et al. (2008), where the fractions have been corrected for background and foreground contamination as well as incompleteness.

Cho et al. (2012) studied the role of environment in galaxy formation and evolution using the GCS of 10 early-type galaxies in low-density environments via deep imaging with the ACS on the Hubble Space Telescope. g and z filters were used and the galaxies studied have magnitudes in the range $-20.33 \leq M_B \leq -18.57$. They concluded that trends in GC properties in the fields are similar to those in dense environments with mean GC color appearing slightly bluer than in dense environments. For similar-luminosity galaxies, field galaxies were found to have lower fraction of red GCs compared to galaxies in clusters. Using simple stellar population models, they found that GCs in fields are either younger or more

metal-poor than those found in dense environments.

Using $(g' - i')$ to $(g - z)_0$ color transformation equation from Usher et al. (2012),

$$(g' - i') = (0.7335 \pm 0.009) \times (g - z)_0 + (0.147 \pm 0.012),$$

we transformed our average colors and sub-population peak colors to $(g - z)_0$ for comparison. We further transformed our colors into metallicity $[Z/H]$ using metallicity-color transformations from Faifer et al. (2011)

$$[Z/H] = (3.51 \pm 0.21) \times (g' - i') - 3.91 \pm 0.20$$

and

$$[Z/H] = (2.56 \pm 0.09) \times (g - z) + (-3.50 \pm 0.11)$$

from Usher et al. (2012). These transformation equations are from studies of GCS. Faifer et al. (2011) conducted deep GMOS photometry for the GCS of five elliptical galaxies in the g', r' and i' filter passbands. Magnitude range, M_B of early type galaxies studied is within the range $-21.43 \leq M_B \leq -19.94$. Only one of the galaxies studied, NGC 3115, belongs to the field environment. Usher et al. (2012) assembled the largest sample of spectroscopic GC metallicity by studying 11 nearby galaxies with a range of galaxy luminosity and environments. They used wide-field photometry results obtained with different instruments in g', r' and i' passbands.

We further use

$$D = \frac{\mid \mu_{\rm blue} - \mu_{\rm red} \mid}{\sqrt{(\sigma^2{}_{blue} + \sigma^2{}_{red})/2}}$$

from Muratov & Gnedin (2010) to estimate peak separation.

For ease of comparison, we compare our results separately with results from Peng et al. (2006) and Cho et al. (2012) in Fig. 17 and Fig. 18. Colors are given in $(g - z)$ and for

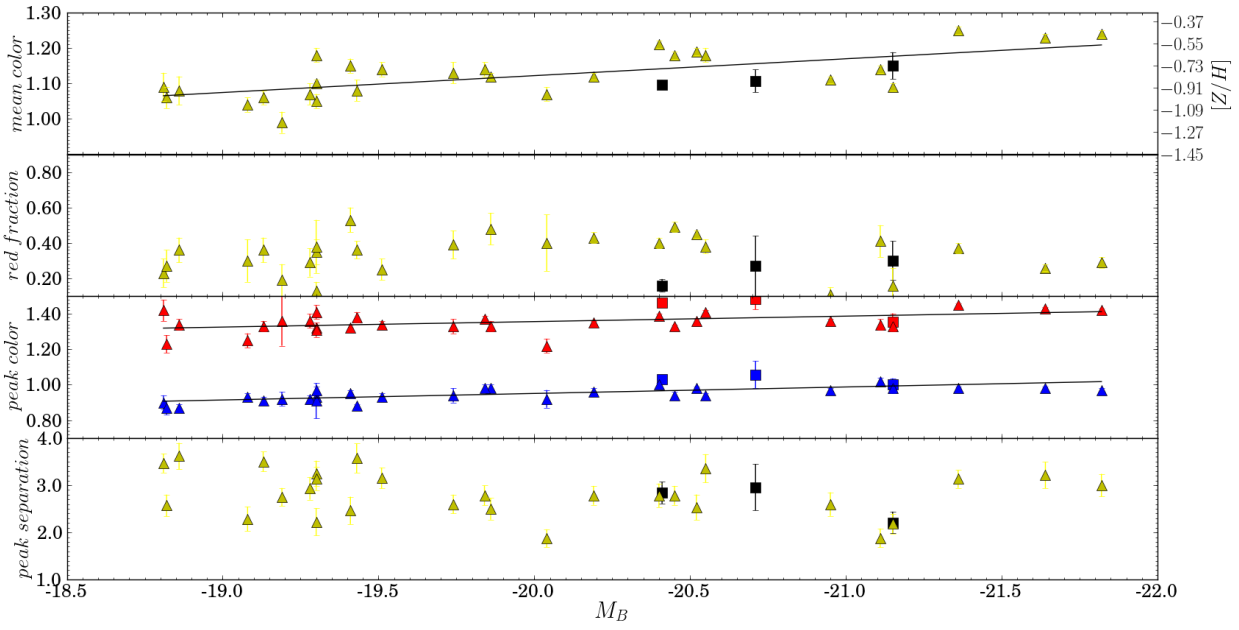

Figure 17: Comparison of GC properties in our sample with Peng et al. (2006) with host galaxy luminosity. From top panel downwards, we compare mean color in $(g-z)_0$, red fraction detected in GCS (Peng et al. 2008), peak color in blue and red sub-populations (also in$(g-z)_0$) and peak separation with local galaxy density. Black and yellow markers represent data from our sample and Peng et al. (2006) respectively. Red and blue markers in peak color vs luminosity plot represent red and blue peaks, with triangles representing data from Peng et al. (2006) and squares, our results

NGC 2865, we treat the very blue subgroup as part of the blue subgroup. The top panels of Fig. 17 compare the mean color of the detected GCs in our sample and Peng et al. (2006) with host galaxy luminosity. We find that generally, mean GC color increases with galaxy luminosity even in GCS of isolated ellipticals. Top panel of Fig. 18 also shows this trend. Also, for a given luminosity, mean color is generally bluer in GCS of isolated ellipticals compared to those from dense environments. Our sample also has a bluer mean GC trend compared with results from Cho et al. (2012) where conditions for definition of galaxy isolation are not as stringent. The straight line is a least square fit to the data.

The second panels of Fig. 17 and Fig. 18 compare the fraction of red clusters detected with host galaxy luminosity. As shown by Cho et al. (2012) for the ACS Virgo cluster survey,

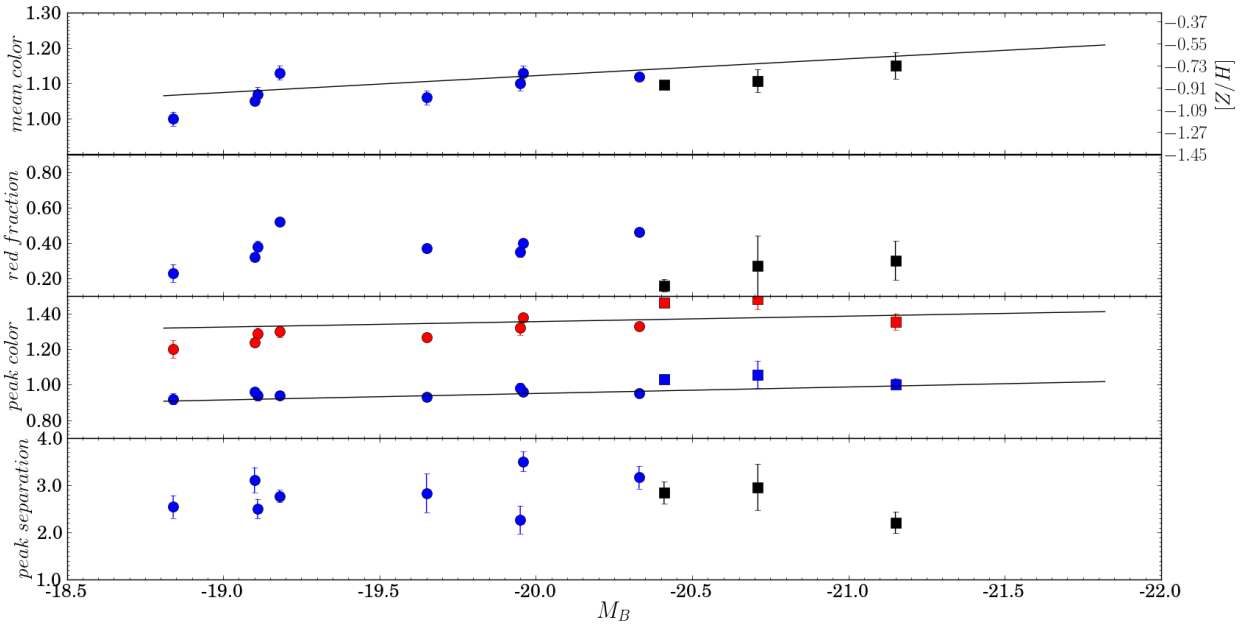

Figure 18: Comparison of GC properties in our sample with Cho et al. (2012) with host galaxy luminosity. From top panel downwards, we compare mean color in $(g-z)_0$, red fraction detected in GCS, peak color in blue and red sub-populations (also in$(g-z)_0$) and peak separation with local galaxy density. Black and blue markers represent data from our sample and Cho et al. (2012) respectively. Red and blue markers in peak color vs luminosity plot represent red and blue peaks, with circles representing data from Cho et al. (2012) and squares, our results

any bias towards the more centrally distributed red GCs due to the smaller area covered by the photometry of NGC 2271 is systematically small even though NGC 2271 is approximately twice as distant as the Virgo cluster. Our GCSs appear to have a smaller fraction of red GCs $(0.16-0.30)$ compared to the low-luminosity, low-density sample of Cho et al. (2012) with NGC 2271, the least luminous, nearest and most extended member of our sample being more dominated by metal-poor GCs. From the analysis of the radial distribution of GCs in our sample, (see Section 3.2), GMOS FOV extends well to the outer regions of NGC 2271, unlike in NGC 3962 and NGC 2865, where there seems to be a bias against GCs in the outer regions. For the high luminosity galaxies in Peng et al. (2006) and in our sample, metal-poor

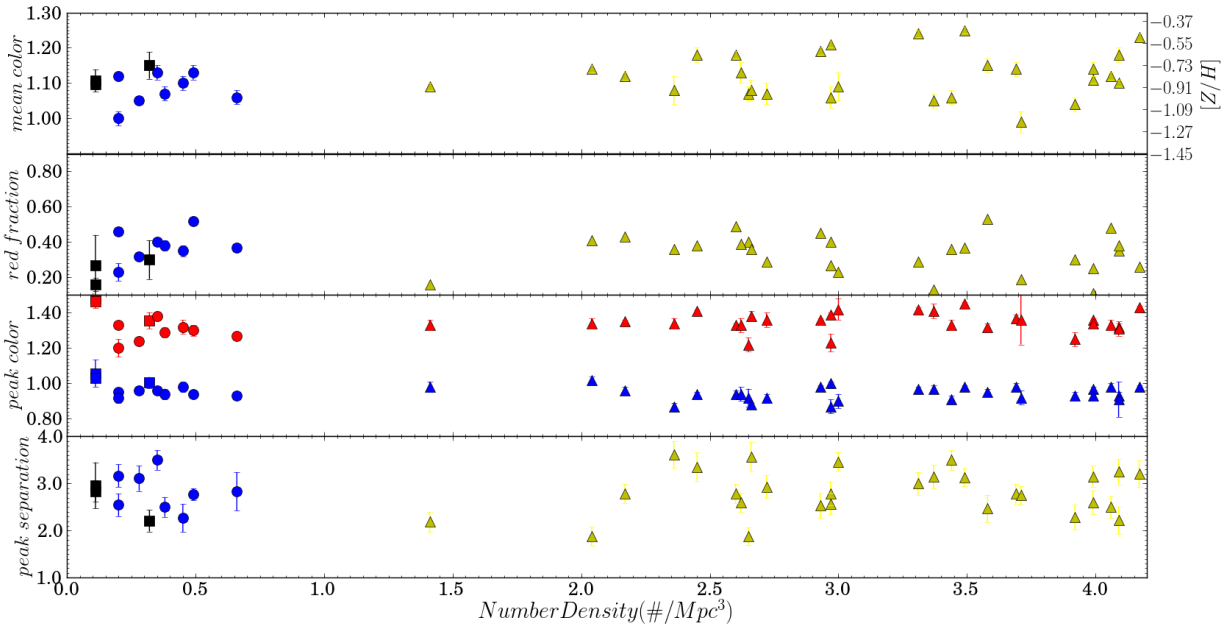

Figure 19: Comparison of GC properties in our sample with Cho et al. (2012) and Peng et al. (2006) with local galaxy density from Tully (1988). From top panel downwards, we compare mean color in $(g-z)_0$, red fraction detected in GCS, peak color in sub-population and peak separation with local galaxy density. Black, blue and yellow markers represent data from our sample, Cho et al. (2012) and Peng et al. (2006) respectively, with triangles corresponding to Peng et al. (2006), circles to Cho et al. (2012) and squares to our results respectively.

clusters dominate the GCS.

Also, there is little difference in the distribution of red fraction between the low-density sample of Cho et al. (2012) and the low luminosity galaxies in Peng et al. (2008). This suggests that environment is not as strong a factor like luminosity in determining what sub-population dominates the GCS.

In the third panels of Fig. 17 and Fig. 18, we compare the peak colors of the blue and red sub-populations in the three samples with host galaxy luminosity. We perform least squares best fits to the blue and red peaks and find that the slope of the red peaks with respect to the galaxy absolute magnitude is steeper than that of the blue peaks in both figures. Blue peaks increase much more slowly with increasing host galaxy absolute magnitude than red peaks in all the three samples. In the last panels, we compare the peak separation in our sample with

peak separations in our comparison samples as a function of host galaxy luminosity. Peak separation is a measure of the strength of bimodality in GCS and according to Muratov & Gnedin (2010), bimodality is strong if peak separation > 2. No clear trend is visible, even though we observe that bimodality is strong in all the three galaxies in our sample.

In Fig. 19, we compare results in our sample with our comparison samples as a function of local galaxy density. Easily, GCS in low-density environment and isolated ellipticals stand out distinct from those from the dense Virgo cluster environment. Trends in variation of GC properties are however not obvious, especially in the first three panels. For example, in the plot of red fraction against local galaxy density, very low red fraction are observed at low density in GCS of NGC 2271 and at comparatively high densities in VGC 2000 and 1938. However in the last panel, strength of bimodality decreases in the under-dense environment as local density increases though this trend is not obvious in the high density environment.

It would seem that there is a complex relationship between observable GC properties and local galaxy environment that is not easily explained due to the rarity of true isolated ellipticals galaxies, especially those with low luminosities though Hernández-Toledo et al. (2008) and Niemi (2011) predicted that blue, dim, faint isolated galaxies should exist in the field. These are yet unobserved.

Even though the peak colors of the red sub-populations in our sample are redder than those of our comparison samples, the mean color of our GCS are slightly bluer at a given luminosity. Thus it would appear that mean colors of GCs in isolated ellipticals are bluer than in denser environments. Interpreting this color offset is tricky, especially with just one color, due to the age-metallicity degeneracy. Cho et al. (2012) attempted to explain the color offset observed between their low-density, low luminosity sample and the high-density sample of Peng et al. (2006) using simple stellar population (SSP) models. A color offset in $(g - z)$ of ~ 0.05 was observed and they tentaively concluded, based on analysis with SSP models, that GCs in low-density environments are either younger ($\triangle age > 2$ Gyr) or more

metal-poor ($\triangle[Fe/H] \sim 0.10 - 0.15$). Comparing the mean color of our sample with that of Peng et al. (2006), we obtain a color offset, again in $(g - z)$, of 0.01. Thus, for a given luminosity, mean color of GCS in isolated and dense environments are similar.

Using the SSP model of Girardi et al. (2004), we plot predicted age and color over the metallicity range of our sample in Fig. 20. Isochrones with corresponding metallicities are also shown. The narrow range of blue peaks and the wider distribution of red peaks from our sample with average $(g' - i')$ colors of 0.90 and 1.20 are shown as overplots of blue and red stripes. This would suggest that the blue sub-populations were all formed from gas materials with same degree of enrichment under similar conditions. In case of the red sub-populations, the wider distribution of the absolute color values highlight the different extent of processing the gas materials would undergo before onset of red cluster formation after truncation of reionization (Griffen et al. 2010). Most GCs in massive galaxies are old objects (Brodie & Strader 2006). Using a conservative lower limit of 8 Gyrs, we find a minimum age difference of 1.5 Gyrs between blue and red sub-populations in the GCS of isolated elliptical galaxies.

4.2 Effects of galaxy evolution on GCS in isolated elliptical galaxies

Isolated ellipticals are expected to evolve passively since they are expected to have evolved with negligible external influences since formation early in cosmic time. This is however not a complete picture of what we see. For example, NGC 2865, a truly isolated elliptical galaxy, is known to have had a recent minor merger. Apart from modifications to the morphology of this galaxy, this is reflected in the GCS as a distinct, very blue, young group of GCs evenly distributed along the plumes, such that it is no longer sufficient to describe its GCS with two modes. Also NGC 3962 has a rather high cold gas content ($2.7 \times 10^9 M_\odot$ Serra & Oosterloo 2010), probably the result of a cold gas accretion from the intergalactic medium or cooling

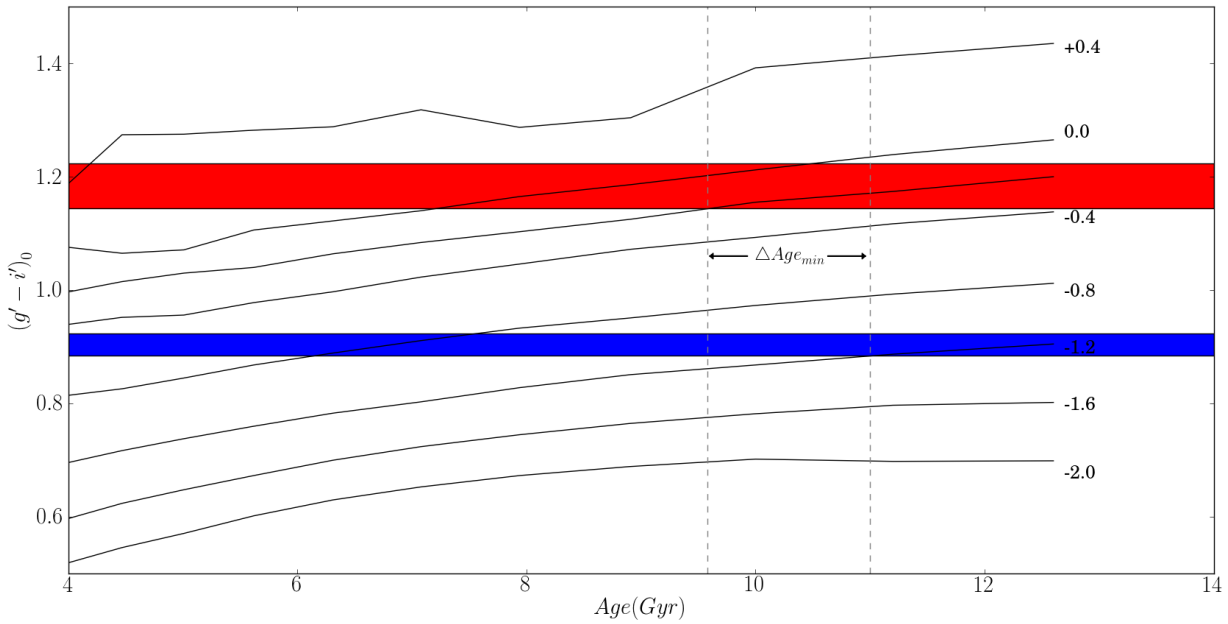

Figure 20: $(g'-i')$ evolution with age at different metallicities using simple stellar population model of Girardi et al. (2004). Metallicity is in [Fe/H] and the two stripes represent the color ranges of the blue and red peaks in our sample. The dashed vertical lines are used to evaluate age difference between the sub-populations assuming they are all old objects.

of hot gas component (Putman et al. 2009) and this reflects in the GCS as a small, distinct group of very blue objects with $(g'-i')$ color between $0.4-0.6$. More tests would be needed to further investigate these rather active evolution scenarios in samples of isolated ellipticals.

Chapter 5

Summary and conclusions

Deep GMOS g' and i' photometry has been done on the GCS of three isolated elliptical galaxies. The main results of this study are:

- All GCS studied have $(g' - i')$ color distributions better described by bimodal Gaussian distribution rather than unimodal model with NGC 2865 showing evidence of a third color mode.

- The peak colors of the red sub-population in all our GCS ($(g' - i') = 1.15$, 1.24 and 1.22 for NGC 3962, NGC 2865 and NGC 2271 respectively) are slightly redder than in GCS of similar mass galaxies in different environments reported in literature.

- The blue sub-population dominates the GCS in the three isolated elliptical galaxies studied with fractions 0.70, 0.73 and 0.84 in NGC 3962, NGC 2865 and NGC 2271 respectively. This is at odds with the hierarchical based model of Tonini (2013) where high-red fractions are expected for isolated elliptical galaxies.

- A population of UCD candidates (resolved and unresolved) were detected in NGC 3962. Spectroscopic studies to determine their membership via radial velocities have been scheduled in the Spring of 2013.

- Sub-populations in our sample have similar spatial distribution with results from literature with the metal-rich GCs having a more central distribution and the metal-poor clusters showing a more extended distribution. Also, we obtained shallow, negative mean GC color gradients in all the three galaxies studied.

Metal poor GCs are first formed at high redshift from primordial gas alongside field stars, they however survive the dynamic evolution of their host galaxy due to their compactness. Reionization in local universe truncates GC formation. However, reionization is inhomogenous in the local universe, propagating from dense regions to under-dense environments (Spitler et al. 2012) such that galaxies in low density environments have longer time to synthesize more metal-poor GCs. This would account for the ***low fraction of red GCs in all GCS in our sample*** and in most GCS in the sample of Cho et al. (2012).

From our analysis using the SSP model of Girardi et al. (2004), we obtained a ***minimum age difference of 1.5 Gyrs between sub-populations in GCS of truly isolated elliptical galaxies***. This is lower than the minimum age difference of 2 Gyrs obtained by Cho et al. (2012). This can be accounted for by the duration of reionization epoch which we would expect to be shorter in our samples (Spitler et al. 2012) compared to denser environments. Hence, in our sample, red GCs begin to form at relatively high redshift from the enriched gas in the host galaxies at the end of the reionization epoch. Evidence of this is seen in the ***relatively higher values of red sub-population peak values*** we obtained in our analysis which can be accounted for by prolonged self-enrichment.

The most visible effects of the under-dense environment of our sample are in the smaller age difference between the blue and red sub-populations and the relatively higher peak $(g' - i')$ ***colors of the metal-rich sub-population. These features cannot be reproduced by luminosities***, hence we tentatively conclude that these are the true imprints of the under-dense environments on the GCS of isolated elliptical galaxies. More tests, especially for low-luminosity isolated elliptical galaxies, would however be needed to obtain more definite results. Individual evolution history of each galaxy affects the GCS even though the galaxies are in the field.

Bibliography

Aars C.E., Marcum P.M., Fanelli M.N., 2001, AJ, 122, 2923

Armandroff T.E., Zinn R., 1988, AJ, 96, 92

Ashman K.M., Zepf S.E., 1992, ApJ, 384, 50

Ashman K.M., Zepf S.E., 1998, Globular Cluster Systems, Cambridge University Press, 1998

Ashman K.M., Bird C.M., Zepf S.E., 1994, AJ, 108, 2348

Barmby P., Huchra J.P., Brodie J.P., et al., 2000, AJ, 119, 727

Beasley M.A., Baugh C.M., Forbes D.A., Sharples R.M., Frenk C.S., 2002, MNRAS, 333, 383

Bekki K., Freeman K.C., 2003, MNRAS, 346, L11

Bekki K., Couch W.J., Drinkwater M.J., 2001, ApJ, 552, L105

Bekki K., Forbes D.A., Beasley M.A., Couch W.J., Oct. 2003, MNRAS, 344, 1334

Bertin E., Arnouts S., 1996, A&AS, 117, 393

Bica E., Bonatto C., Barbuy B., Ortolani S., 2006, A&A, 450, 105

Birkinshaw M., Davies R.L., 1985, ApJ, 291, 32

Bragaglia A., Carretta E., Gratton R., et al., 2013, A&A

Brodie J.P., Strader J., 2006, ARA&A, 44, 193

Brodie J.P., Usher C., Conroy C., et al., 2012, ApJ, 759, L33

Buson L.M., Sadler E.M., Zeilinger W.W., et al., 1993, A&A, 280, 409

Caldwell N., Schiavon R., Morrison H., Rose J.A., Harding P., 2011, AJ, 141, 61

Chies-Santos A.L., Larsen S.S., Cantiello M., et al., 2012, A&A, 539, A54

Cho J., Sharples R.M., Blakeslee J.P., et al., 2012, MNRAS, 422, 3591

Cole S., Lacey C.G., Baugh C.M., Frenk C.S., 2000, MNRAS, 319, 168

Côté P., Marzke R.O., West M.J., 1998, ApJ, 501, 554

de Souza R.E., Gadotti D.A., dos Anjos S., 2004, ApJS, 153, 411

de Vaucouleurs G., de Vaucouleurs A., Corwin H.G. Jr., et al., 1991, Third Reference Catalogue of Bright Galaxies. Volume I: Explanations and references. Volume II: Data for galaxies between 0^h and 12^h. Volume III: Data for galaxies between 12^h and 24^h, Springer, New York, NY (USA), 1991, 2091 p.

Di Matteo P., Pipino A., Lehnert M.D., Combes F., Semelin B., 2009, A&A, 499, 427

Dirsch B., Richtler T., Geisler D., et al., 2003, AJ, 125, 1908

Djorgovski S., Santiago B.X., 1992, ApJ, 391, L85

Dressler A., 1980, ApJ, 236, 351

Elmegreen B.G., Jan. 2008, ApJ, 672, 1006

Faifer F.R., Forte J.C., Norris M.A., et al., 2011, MNRAS, 416, 155

Fall S.M., Zhang Q., 2001, ApJ, 561, 751

Fleming D.E.B., Harris W.E., Pritchet C.J., Hanes D.A., 1995, AJ, 109, 1044

Forbes D.A., 2005, ApJ, 635, L137

Forbes D.A., Forte J.C., 2001, MNRAS, 322, 257

Forbes D.A., Brodie J.P., Grillmair C.J., 1997, AJ, 113, 1652

Forbes D.A., Faifer F.R., Forte J.C., et al., 2004, MNRAS, 355, 608

Fort B.P., Prieur J.L., Carter D., Meatheringham S.J., Vigroux L., 1986, ApJ, 306, 110

Garcia A.M., 1993, A&AS, 410, 47

Geisler D., Lee M.G., Kim E., 1996, AJ, 111, 1529

Gillessen S., Eisenhauer F., Trippe S., et al., 2009, ApJ, 692, 1075

Girardi L., Grebel E.K., Odenkirchen M., Chiosi C., 2004, A&A, 422, 205

Goudfrooij P., Hansen L., Jorgensen H.E., Norgaard-Nielsen H.U., 1994, A&AS, 105, 341

Griffen B.F., Drinkwater M.J., Thomas P.A., Helly J.C., Pimbblet K.A., 2010, MNRAS, 405, 375

Harris W.E., Pudritz R.E., 1994, ApJ, 429, 177

Harris W.E., van den Bergh S., 1981, AJ, 86, 1627

Hau G.K.T., Forbes D.A., 2006, MNRAS, 371, 633

Hau G.K.T., Carter D., Balcells M., 1999, MNRAS, 306, 437

Hau G.K.T., Spitler L.R., Forbes D.A., et al., 2009, MNRAS, 394, L97

Hernández-Toledo H.M., Vázquez-Mata J.A., Martínez-Vázquez L.A., et al., 2008, AJ, 136, 2115

Hilker M., Richtler T., 2000, A&A, 362, 895

Hilker M., Infante L., Richtler T., 1999, A&AS, 138, 55

Holtzman J.A., Faber S.M., Shaya E.J., et al., 1992, AJ, 103, 691

Izenman A., 1991, Journal of the American Statistical Association, 86, 205

Jordán A., McLaughlin D.E., Côté P., et al., 2006, ApJ, 651, L25

Karachentseva V.E., Lebedev V.S., Shcherbanovskij A.L., Mar. 1986, Bulletin d'Information du Centre de Donnees Stellaires, 30, 125

Kissler-Patig M., Kohle S., Hilker M., et al., 1997, A&A, 319, 470

Koprolin W., Zeilinger W.W., 2000, A&AS, 145, 71

Krauss L.M., Chaboyer B., 2003, Science, 299, 65

Kroupa P., 1998, MNRAS, 300, 200

Kuntschner H., Smith R.J., Colless M., et al., 2002, MNRAS, 337, 172

Lane R.R., Salinas R., Richtler T., 2013, A&A, 549, A148

Larsen S.S., Richtler T., 2000, A&A, 354, 836

Larsen S.S., Brodie J.P., Huchra J.P., Forbes D.A., Grillmair C.J., 2001, AJ, 121, 2974

Liu C., Peng E.W., Jordán A., et al., 2011, ApJ, 728, 116

Malin D.F., Carter D., 1983, ApJ, 274, 534

Markwardt C.B., 2009, In: Bohlender D.A., Durand D., Dowler P. (eds.) Astronomical Data Analysis Software and Systems XVIII, vol. 411 of Astronomical Society of the Pacific Conference Series, 251

McLaughlin D.E., 1999, AJ, 117, 2398

McLaughlin D.E., Secker J., Harris W.E., Geisler D., 1995, AJ, 109, 1033

Metcalfe N., Shanks T., Campos A., McCracken H.J., Fong R., 2001, MNRAS, 323, 795

Meylan G., Sarajedini A., Jablonka P., et al., 2001, AJ, 122, 830

Muratov A.L., Gnedin O.Y., 2010, ApJ, 718, 1266

Murray N., 2009, ApJ, 691, 946

Muzzio J.C., Martinez R.E., Rabolli M., Oct. 1984, ApJ, 285, 7

Niemi S.M., 2011, Properties of Galaxies and Groups: Nature versus Nurture, Ph.D. thesis, University of Turku, Turku

Oser L., Ostriker J.P., Naab T., Johansson P.H., Burkert A., 2010, ApJ, 725, 2312

Ostrov P., Geisler D., Forte J.C., 1993, AJ, 105, 1762

Peng E.W., Jordán A., Côté P., et al., 2006, ApJ, 639, 95

Peng E.W., Jordán A., Côté P., et al., 2008, ApJ, 681, 197

Portegies Zwart S.F., McMillan S.L.W., Gieles M., 2010, ARA&A, 48, 431

Putman M.E., Henning P., Bolatto A., et al., 2009, In: astro2010: The Astronomy and Astrophysics Decadal Survey, vol. 2010 of A&A, 241

Puzia T.H., 2003, Extragalactic Globular Cluster Systems, Ph.D. thesis, Sternwarte München Scheinerstr. 1, 81679 München

Puzia T.H., Kissler-Patig M., Thomas D., et al., 2005, A&A, 439, 997

Reda F.M., Forbes D.A., Beasley M.A., O'Sullivan E.J., Goudfrooij P., 2004, MNRAS, 354, 851

Rejkuba M., 2012, Ap&SS, 341, 195

Rhode K.L., Zepf S.E., 2004, AJ, 127, 302

Richtler T., 2006, Bulletin of the Astronomical Society of India, 34, 83

Richtler T., Salinas R., Misgeld I., et al., 2011, A&A, 531, A119

Schlegel D.J., Finkbeiner D.P., Davis M., 1998, ApJ, 500, 525

Secker J., 1992, AJ, 104, 1472

Serra P., Oosterloo T.A., 2010, MNRAS, 401, L29

Shapley H., 1918, ApJ, 48, 154

Sikkema G., Peletier R.F., Carter D., Valentijn E.A., Balcells M., 2006, A&A, 458, 53

Smith J.A., Tucker D.L., Allam S.S., Jorgensen A.M., 2002, In: American Astronomical Society Meeting Abstracts, vol. 34 of Bulletin of the American Astronomical Society, 104

Smith R.M., Martínez V.J., Graham M.J., 2004, ApJ, 617, 1017

Spitler L.R., Forbes D.A., Strader J., Brodie J.P., Gallagher J.S., 2008, MNRAS, 385, 361

Spitler L.R., Romanowsky A.J., Diemand J., et al., 2012, MNRAS, 423, 2177

Stetson P.B., 1992, In: Worrall D.M., Biemesderfer C., Barnes J. (eds.) Astronomical Data Analysis Software and Systems I, vol. 25 of Astronomical Society of the Pacific Conference Series, 297

Stocke J.T., Keeney B.A., Lewis A.D., Epps H.W., Schild R.E., 2004, AJ, 127, 1336

Strader J., Brodie J.P., Forbes D.A., 2004, AJ, 127, 3431

Strader J., Brodie J.P., Cenarro A.J., Beasley M.A., Forbes D.A., 2005, AJ, 130, 1315

Strader J., Brodie J.P., Spitler L., Beasley M.A., 2006, AJ, 132, 2333

Tal T., van Dokkum P.G., Nelan J., Bezanson R., 2009, AJ, 138, 1417

Tonini C., 2013, ApJ, 762, 39

Tonry J.L., Dressler A., Blakeslee J.P., et al., 2001, ApJ, 546, 681

Tully R.B., 1988, Nearby galaxies catalog, Cambridge University Press, 1988, 221 p.

Usher C., Forbes D.A., Brodie J.P., et al., 2012, MNRAS, 426, 1475

Valcarce A.A.R., Catelan M., 2011, A&A, 533, A120

Wehner E.M.H., Harris W.E., Whitmore B.C., Rothberg B., Woodley K.A., 2008, ApJ, 681, 1233

Whitmore B.C., Schweizer F., 1995, AJ, 109, 960

Yoon S.J., Lee S.Y., Yi S., Lee Y.W., 2006, In: American Astronomical Society Meeting Abstracts 207, vol. 207 of American Astronomical Society Meeting Abstracts, 128.22

Yoon S.J., Lee S.Y., Blakeslee J.P., et al., 2011a, ApJ, 743, 150

Yoon S.J., Sohn S.T., Lee S.Y., et al., 2011b, ApJ, 743, 149

Zeilinger W.W., Pizzella A., Amico P., et al., 1996, A&AS, 120, 257

Zepf S.E., Ashman K.M., 1993, MNRAS, 264, 611

Zepf S.E., Ashman K.M., English J., Freeman K.C., Sharples R.M., 1999, AJ, 118, 752

Zinnecker H., Keable C.J., Dunlop J.S., Cannon R.D., Griffiths W.K., 1988, In: Grindlay J.E., Philip A.G.D. (eds.) The Harlow-Shapley Symposium on Globular Cluster Systems in Galaxies, vol. 126 of IAU Symposium, 603